Electronic Supplementary Information

N-Functionality Actuated Improved CO_2 Adsorption and Turn-on Detection of Organo-Toxins with Guest-Induced Fluorescence Modulation in Isostructural Diamondoid MOFs

Manpreet Singh,[ab] Athulya S. Palakkal,[c] Renjith S. Pillai*[c] and Subhadip Neogi*[ab]

[a]Inorganic Materials & Catalysis Division, CSIR-Central Salt and Marine Chemicals Research Institute (CSMCRI), Bhavnagar, Gujarat 364002, India
[b]Academy of Scientific and Innovative Research (AcSIR), Ghaziabad- 201002, India
[c]Department of Chemistry, SRM Institute of Science and Technology, Kattankulathur, Tamil Nadu 603203, India
*E-mail (SN): sneogi@csmcri.res.in
*E-mail (RSP): renjiths@srmist.edu.in

Physical Measurements

The infrared spectra (IR) of the samples were recorded using the KBr pellet method on a Perkin–Elmer GX FTIR spectrometer in the region of 400-4000 cm^{-1}. Powder X-ray diffraction (PXRD) data were collected using a PANalytical Empyrean (PIXcel 3D detector) System equipped with Cu Kα (λ=1.54 Å) radiation. Microanalyses of the compounds were Conducted using elementary vario MICRO CUBE analyser. Thermogravimetric analyses (TGA) (heating rate of 5 °C/min under N_2 atmosphere) were performed with a Mettler Toledo Star SW 8.10 system. Surface area measurements of the degassed sample were Carried out using Micromeritics ASAP 2020 analyser. Before adsorption measurement, as synthesized compounds were immersed in dry DCM for three days at room temperature to replace lattice guest molecules. The solvent-exchanged frameworks were then degassed overnight under vacuum at 120 °C to generate **7a** and **8a**. UV-Vis spectra recorded using Shimadzu UV-3101 PC spectrometer and the luminescence experiments were performed at room temperature using a Fluorolog Horiba Jobin Yvon spectrophotometer.

Chemicals

Analytical grade cadmium nitrate hexahydrate $Cd(NO)_3 \cdot 4H_2O$ (AR), N, N′-dimethylformamide (DMF), dichloromethane (DCM) (Fisher Scientific), methanol (S. D. Fine Chemicals, India), were purchased and used without any further purification. Ligand 4-(1H-1, 2, 4-triazol-1-yl) benzoic acid (PTBA) and 4-(1H-imidazol-1-yl)benzoic acid (HIBA) was synthesised as mentioned in experimental section. All the aminophenolic compounds and pesticides used for the sensing experiments were procured commercially and used without any further analysis.

Single Crystal X-ray Crystallography

Single crystals with suitable dimensions were chosen under an optical microscope and mounted on a glass fibre for data collection. Intensity data for as synthesized colorless crystals of **CSMCRI-7 and CSMCRI-8** were collected using graphite-monochromated MoK_α (λ=0.71073 Å) radiation on a Bruker SMART APEX diffractometer equipped with CCD area detector at 173 K, The linear absorption coefficients, scattering factors for the atoms, and the anomalous dispersion corrections were taken from International Tables for X-ray Crystallography. The data integration and reduction were performed with SAINT software.[1] Absorption corrections to the collected reflections were accounted with SADABS[2] using XPREP.[1, 3] The structure was solved by direct method using SIR-97[4] and was refined on F^2 by the full-matrix least-squares technique using the SHELXL-2014[5] program package. All H atoms were placed in calculated positions using idealized geometries (riding model) and assigned fixed isotropic displacement parameters using the SHELXL default. To give an account of disordered electron densities associated with solvent molecules, the "SQUEEZE" protocol in PLATON[6] was applied that produced a set of solvent free diffraction intensities. Final cycles of least-squares refinements improved both the R values and Goodness of Fit with the modified data set after subtracting the contribution from the disordered solvent molecules, using SQUEEZE program. The crystal and refinement data for solvent free **CSMCRI-8** is listed in **Table S4**. Topological analysis was performed by using TOPOS software.[7, 8]

Luminescence Sensing Experiments.

The activated frameworks **7a** and **8a** were finely grounded and well dispersed in DMF medium (1 mg in 2 mL of DMF) under ultrasonication for one hour. For aminophenols sensing experiments, DMF solutions of aminophenols were prepared. All measurements were performed at room temperature. For pesticides sensing experiments, 5 mM stock solutions of pesticides were prepared in DMF solutions. All the measurements for sensing experiments were performed at room temperature.

Typical Procedure for Fluorescence Titration Studies.

The powder sample of **7a** and **8a** were dispersed to form a suspension and subsequently transferred to a quartz cuvette of 1 cm path length. Fluorescence titrations were carried out by incremental addition of the freshly prepared analyte solutions to the dispersion under stirring condidtions. After recording the emission spectra of bare dispersion, the subsequent FL spectra were recorded immediately after addition of the analytes, and during the whole period of performing each titration, the solution was continuously stirred to maintain the uniformity of the dispersion. All titrations were performed in triplicate, and consistent results were reported.

Recyclable Luminescence Experiments. The reproducibility of **8a** toward sensing of DEP, IPT and dichloran was studied. After the first sensing experiment, the MOF powder was recovered by centrifugation and washed with DCM several times. Subsequently, the material was air-dried and used for the next cycle of experiments.

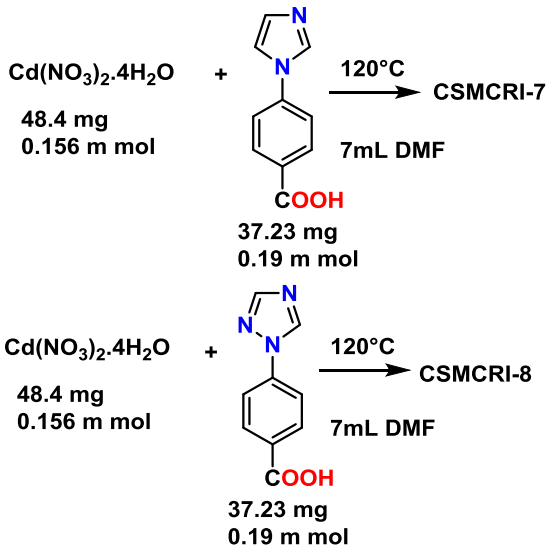

Scheme S1. Synthetic scheme of the MOFs [Cd(***L1***)$_2$]·2DMF (**CSMCRI-7**) and [Cd(***L2***)$_2$]·2DMF (**CSMCRI-8**)

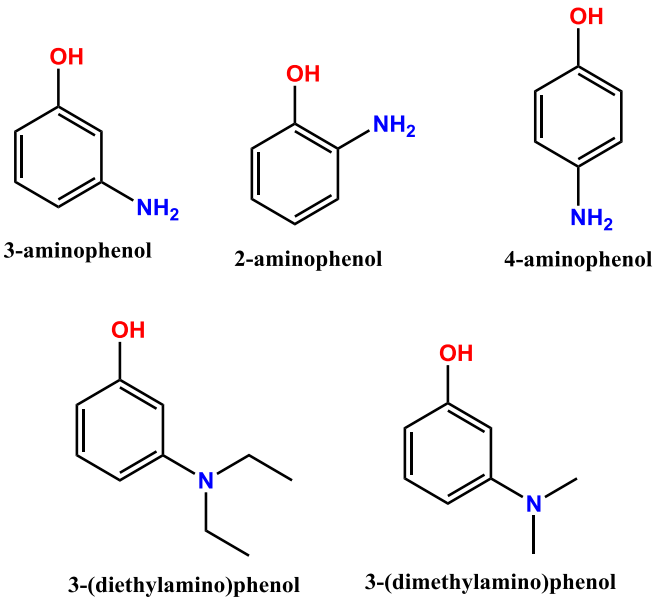

Scheme S2. Chemical structures of aminophenols used for sensing studies.

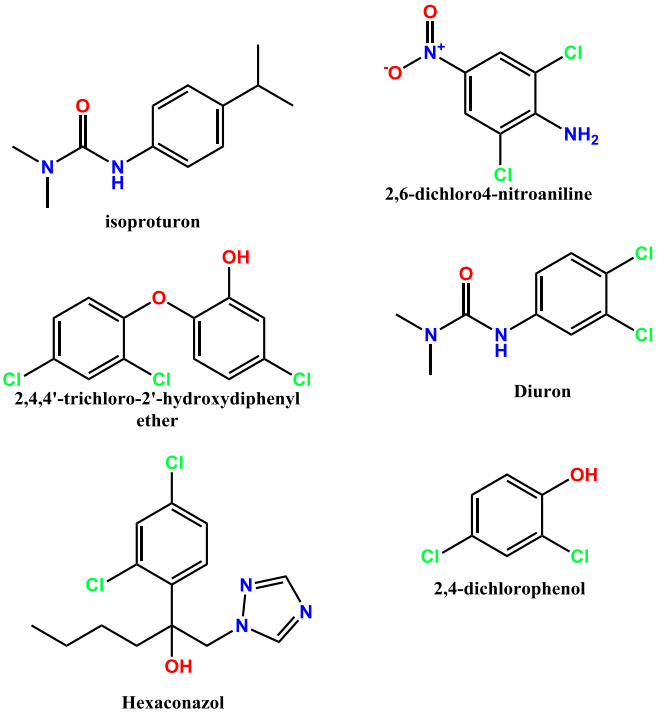

Scheme S3. Chemical structures of pesticides used for sensing studies.

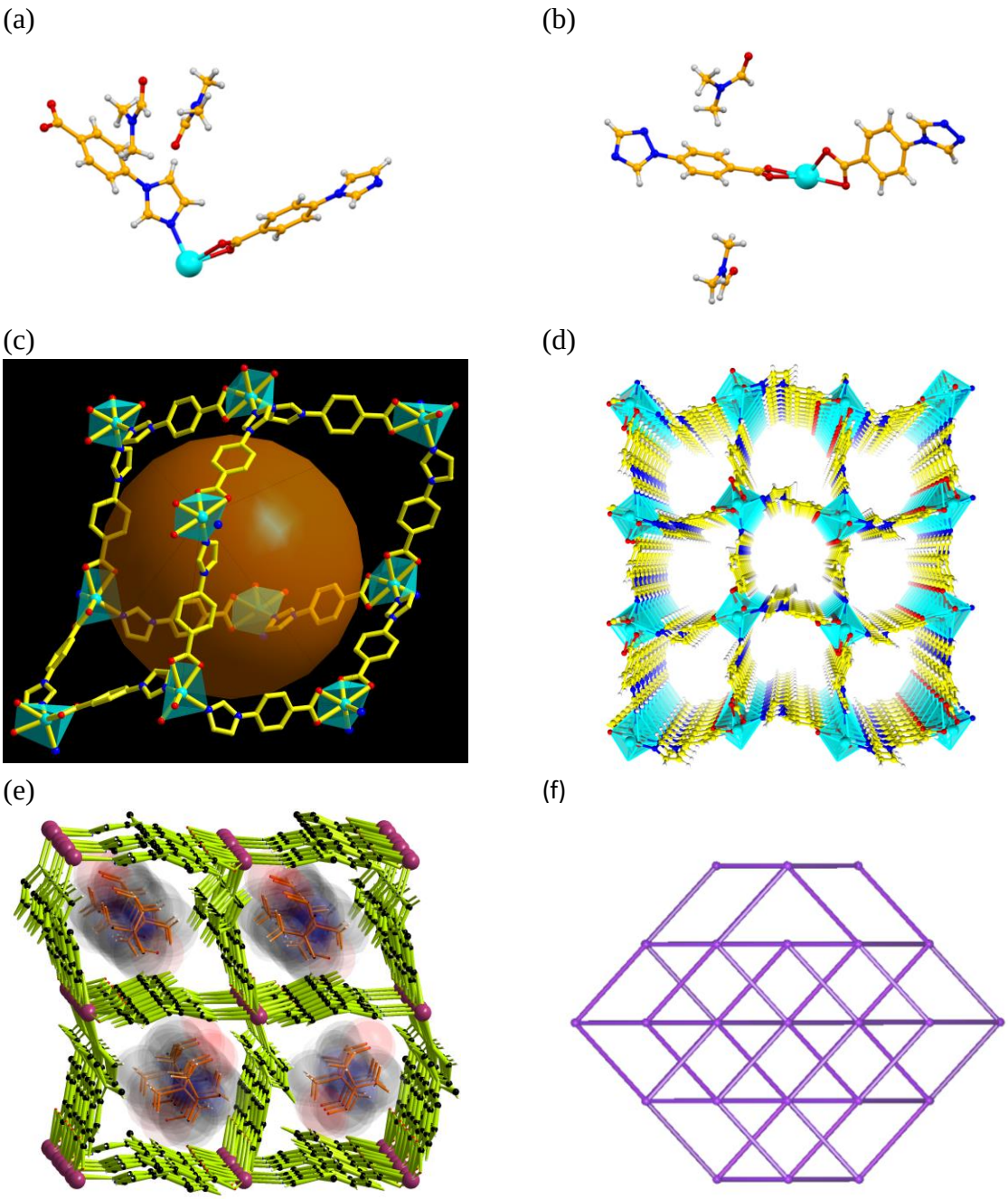

Fig. S1. Asymmetric unit of (a) **CSMCRI-7**, and (b) **CSMCRI-8**, (c) single diamondoid cage in **CSMCRI-7**, and (d) perspective view of pores channels. The view of (e) 3D structure of **CSMCRI-7**, containing DMF guests, and (f) the topological representation of the diamondoid net.

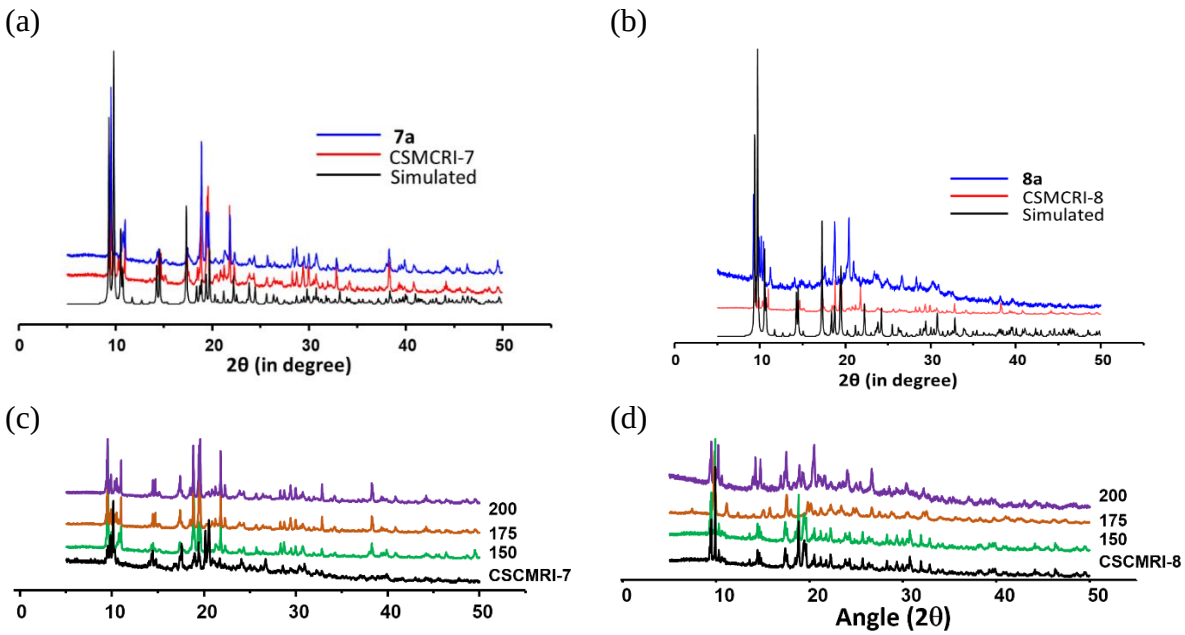

Fig. S2. Simulated (black), experimental (red), and desolvated (blue) PXRD patterns for (a) **CSMCRI-7** and (b) **CSMCRI-8** and variable temperature PXRD patterns of (c) **CSMCRI-7** and (d) **CSMCRI-8**.

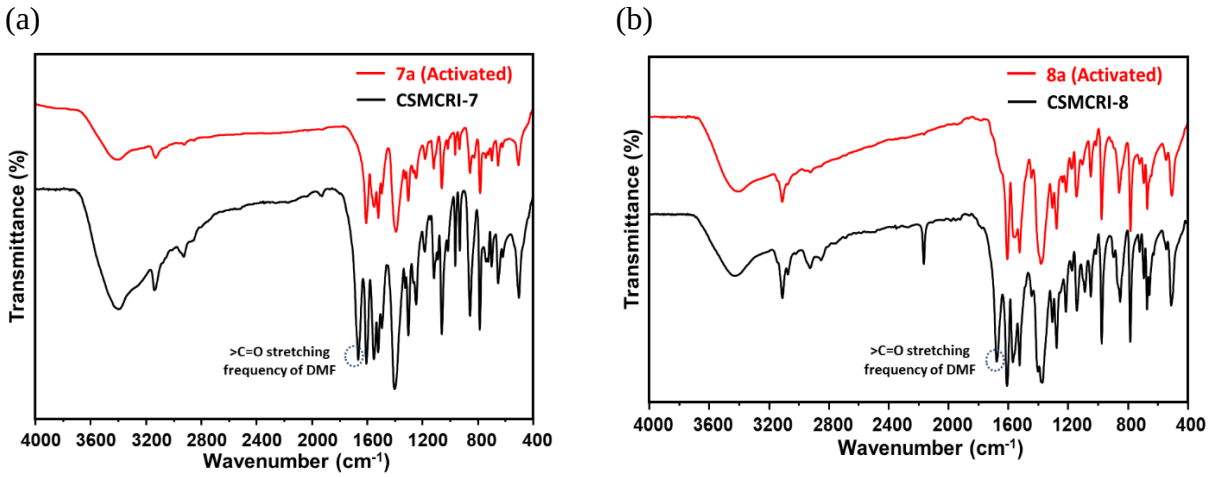

Fig. S3. FT-IR spectra (KBr pellets, cm^{-1}) of (a) **CSMCRI-7** (black) and **7a** (red) and (b) **CSMCRI-8** (black) and **8a** (red)

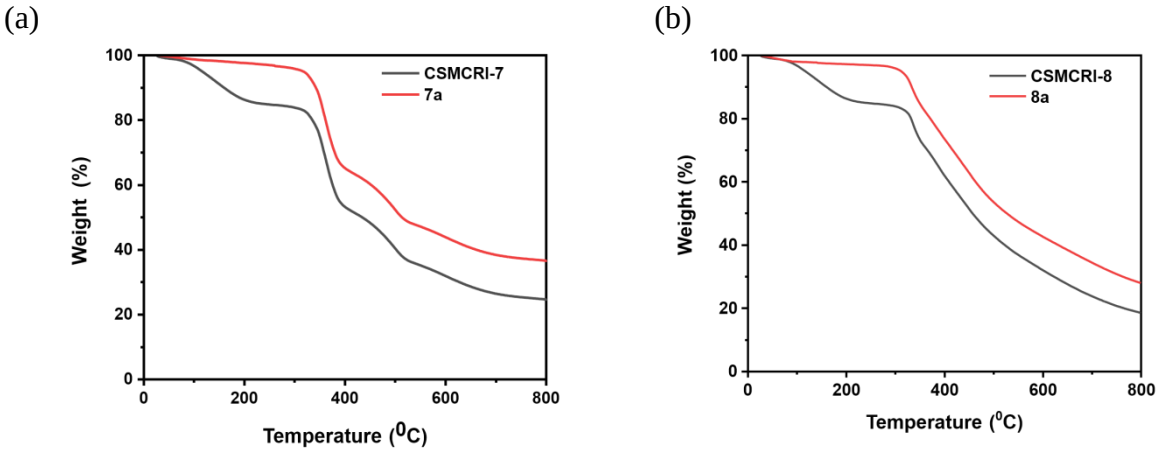

Fig. S4. Thermogravimetric analysis of (a) **CSMCRI-7** and **7a** and (b) **CSMCRI-8** and **8a**.

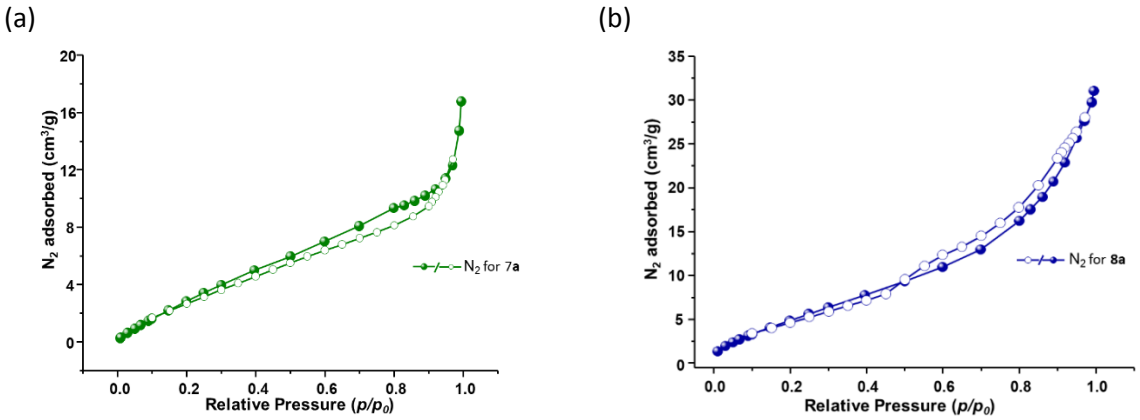

Fig. S5. N_2 Adsorption isotherms of (a) **7a** and (b) **8a** at 77K.

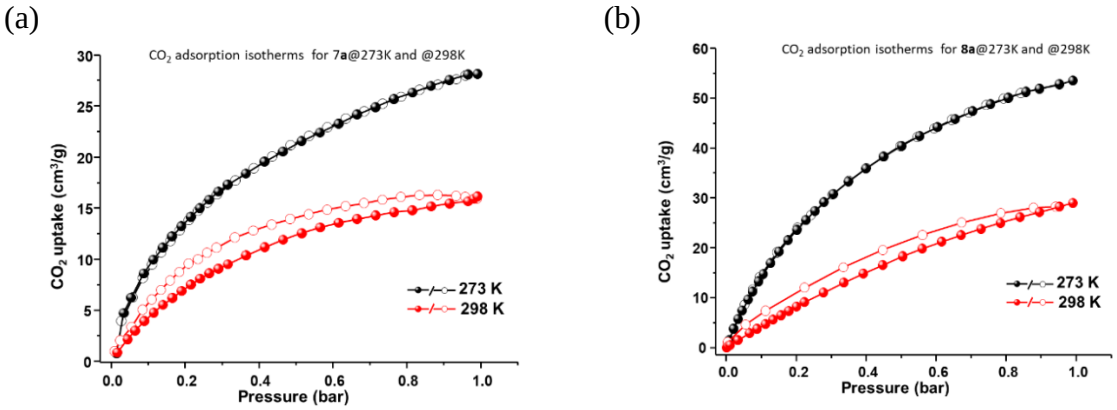

Fig. S6. CO_2 adsorption isotherms of (a) **7a** and (b) **8a** at 273 K and 298 K. Filled circle represents adsorption and empty circle represents desorption.

Calculation of Heat of Adsorption (Q_{st})

Heat of adsorption was calculated using Clausius Clapeyron equation. Two sets of data points were recorded for both temperature and pressure are required respectively. CO_2 adsorption isotherms data at 273 K & 298 K in the pressure range from 0-1 bar with constant uptake was recorded and fitted in the equation.

$$ln\frac{P_2}{P_1} = \frac{\Delta H_{ads}}{R}\left(\frac{T_2 - T_1}{T_2 T_1}\right)$$

Where,

ΔH_{ads} = Isosteric heat of adsorption,
R = universal gas constant,
P = pressure,
T = temperature.

The ΔH_{ads} is obtained as a function of uptake by using above equation and adsorption isotherms measured as shown in main text and this was carried out with a linear interpolation method, as shown below.

Calculations of Adsorption Selectivity by IAST method

Ideal Adsorption Solution Theory (IAST) was employed to predict mixed-gas adsorption equilibria from single component isotherms. Prior to perform the calculations, the single-component isotherms should be fitted by a proper model and numerous methods are available. Data were fitted in Langmuir-Freundlich model of adsorption.

$$y = \frac{q(kx^n)}{(1 + kx^n)}$$

The inputs to the IAST calculations are pure-component adsorption isotherms at the temperature of interest, and the output is the adsorption selectivity is defined by the following equation,

$$S_{ads} = \frac{q_{CO_2}/q_{Other\ gas}}{p_{CO_2}/p_{other\ gas}}$$

Where, q_{CO_2} and $q_{Other\ gas}$ are the absolute component loadings of the adsorbed phase in the mixture and p_{CO_2} and $p_{other\ gas}$ are the corresponding relative pressure.

Table S1 Fitting parameters for **7a** and **8a**

Gas	Fitting Parameters	7a	8a
	Adj. R-square	0.99	0.99
CO_2	**q**	51.76	84.95
	k	1.27	1.80
	n	0.7594	0.9437
N_2	**q**	0.55	0.62
	k	9.97	14.49
	n	2.99	3.33
CH_4	**q**	19.07	29.26
	k	1.13	0.74
	n	1.01	1.14

Computational Modelling Part
Microscopic Models for the Host Framework.

The experimentally elucidated structure of **7a** and **8a** were initially geometry optimized at the Density Functional Theory (DFT) level using the CP2K package.[9] In these simulations, the positions of atoms of the framework were relaxed while the unit cell parameters were kept fixed at the values determined experimentally. All the structural optimizations were done using Perdew-Burke-Ernzerhof (PBE)[10] functional along with a combined Gaussian basis set and pseudo potential. For Carbon, Nitrogen, Oxygen, and Hydrogen, a triple zeta (TZVP-MOLOPT) basis set was considered, while a double zeta (DZVP-MOLOPT) was applied for Cadmium.[11] The pseudo potentials used for all of the atoms were those derived by Goedecker, Teter and Hutter.[12] The van der Waals effects interactions were taken into account via the use of semi-empirical dispersion corrections as implemented in the DFT-D3 method.[13] The atomic point charges for all framework atoms in **7a** and **8a** (Fig. S7) were obtained using the REPEAT method proposed by Campana et al.,[14] which was recently implemented into the CP2K code based on a restrained electrostatic potential framework.[15]

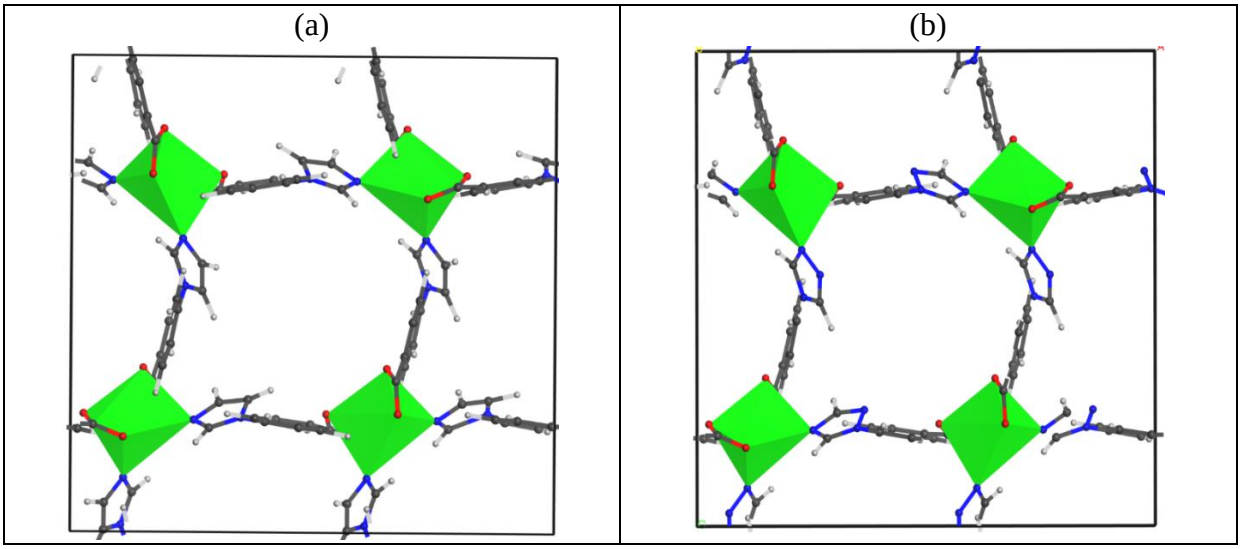

Fig. S7. The single unit cell (1×1×1 simulation box), considered for the DFT calculations viewed along *c* for (a) **7a** and (b) **8a** (right). (black, carbon; grey, hydrogen; red, oxygen; green, Cadmium).

Force Fields

The interaction between the **MOF** frameworks (**7a** and **8a**) and the guest molecules were modelled using the sum of a 12-6 Lennard-Jones (LJ) contribution and a columbic term. The Universal force field (UFF) and DREIDING was adopted to describe the LJ parameters for the respective inorganic and organic part of the atoms in the MOF framework[16,17] (**Table S2**). In this work, CO_2 has been modelled as a rigid molecule through the EPM2 intermolecular potential[18].

Table S2 LJ potential parameters for the atoms of the **7a** and **8a**

Atomic type	**DREIDING**	
	σ **(Å)**	ε **/k$_B$ (K)**
C	3.473	47.860
H	2.844	7.6490
O	3.033	48.158
N	3.662	34.724
Cd	2.848	114.735

Table S3. Potential parameters and partial charges for the adsorbates

Atomic type	σ **(Å)**	ε **/k$_B$ (K)**	q **(*e*)**
CO2_C	2.757	28.129	0.6512
CO2_O	3.033	80.507	-0.3256

GCMC Simulations

Grand Canonical Monte Carlo (GCMC) simulations were performed using the RASPA simulation code.[19] The simulation box was made of 8 (2×2×2) and 12 (2x3x2) unit cells of **7a** and **8a** respectively. Short-range dispersion forces were truncated at a cutoff radius of 12 Å while the interactions between unlike force field centres *a* and *b* were treated by means of the Lorentz-Berthelot combination rules; $\varepsilon_{ab} = \sqrt{\varepsilon_a \varepsilon_b}$, $\sigma_{ab} = (\sigma_a + \sigma_b)/2$, where ε_a and σ_a are the LJ parameters for the species *a*. The long-range electrostatic interactions were handled using the Ewald summation technique. The fugacities for each adsorbed species at a given thermodynamic condition were computed with the Peng-Robinson equation of state (EoS).[20] For each state point, 5×10^7 Monte Carlo steps have been used for both equilibration and

production runs. Three types of trials were considered for the molecules: (i) translation or rotation, (ii) creation/deletion and (iii) exchange of molecular identity. The adsorption enthalpy at low coverage (Δh) for each gas was calculated through configurational-bias Monte Carlo simulations performed in the NVT ensemble using the revised Widom's test particle insertion method.[21] Additionally, in order to gain insight into the configurationally distribution of the adsorbed species in **7a** and **8a**, some additional data were calculated at different pressure including the radial distribution functions (RDF) between the guests and the host.

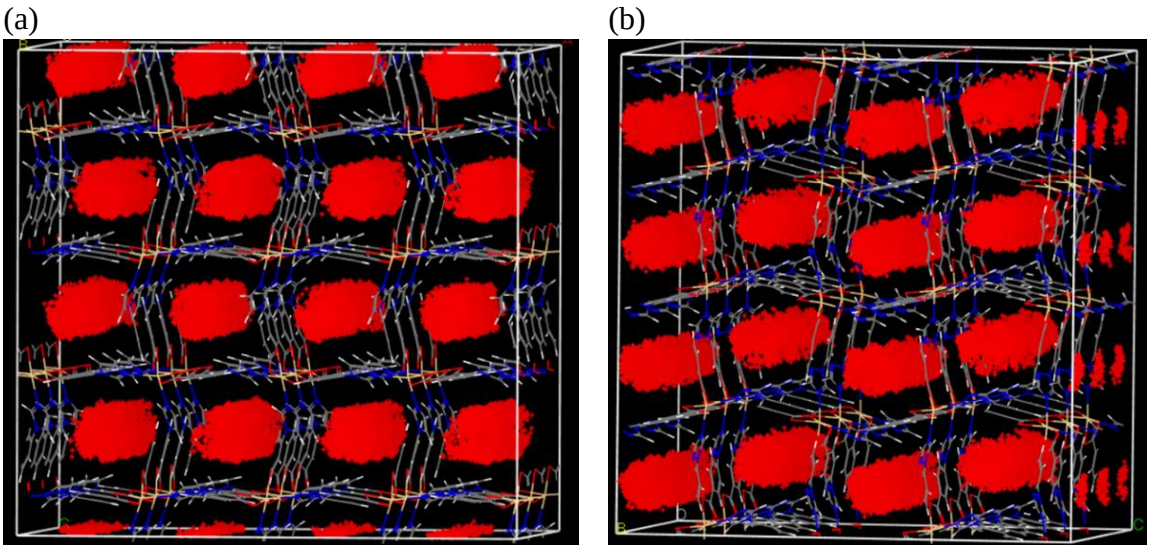

Fig. S8. Maps of the occupied positions of CO_2 (red) in 500 equilibrated frames for a given pressure of 1 bar and at 298 K for **7a** (a) **8a** (b).

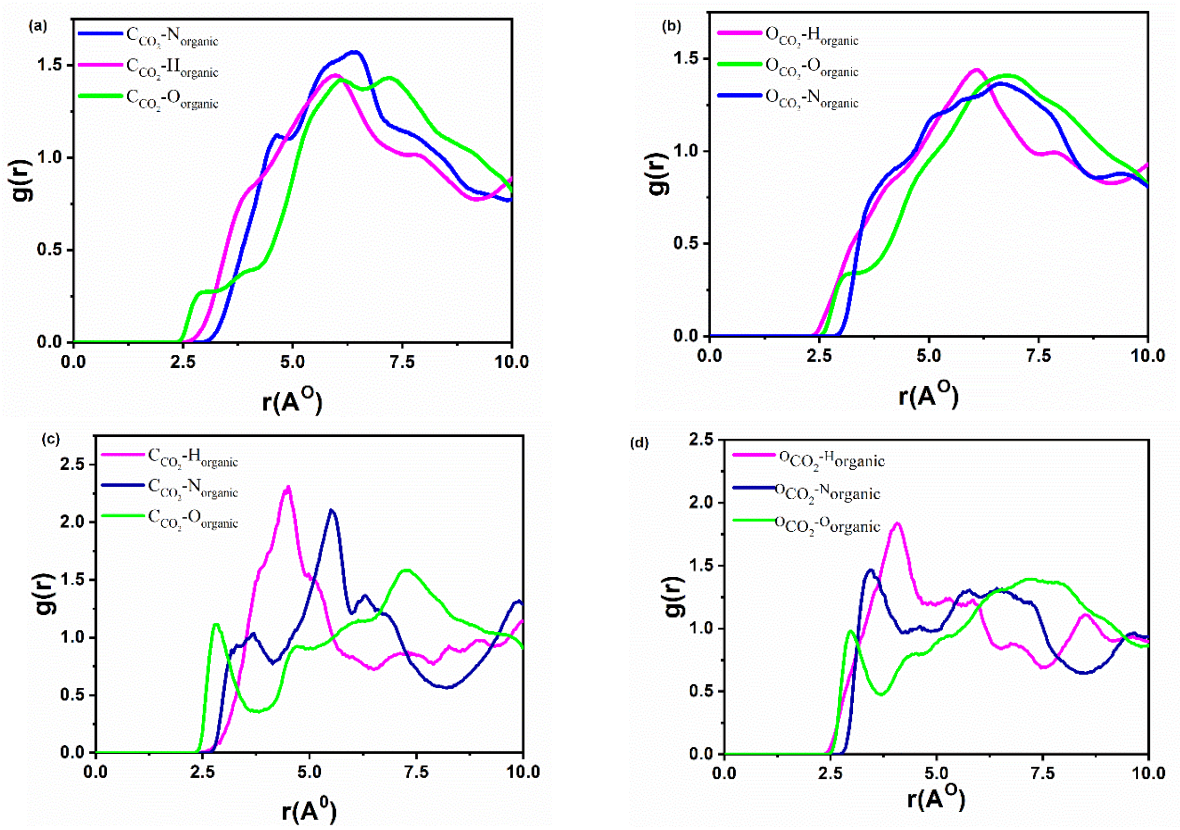

Fig. S9. Radial distribution functions (RDF) between CO_2 and the atoms in the framework (Organic nitrogen, $N_{organic}$: blue, Organic hydrogen, $H_{organic}$: Magenta and Organic Oxygen, $O_{organic}$: green) extracted from the single component adsorption in **7a** (a&b) and **8a** (c&d) at 1 bar and 298 K).

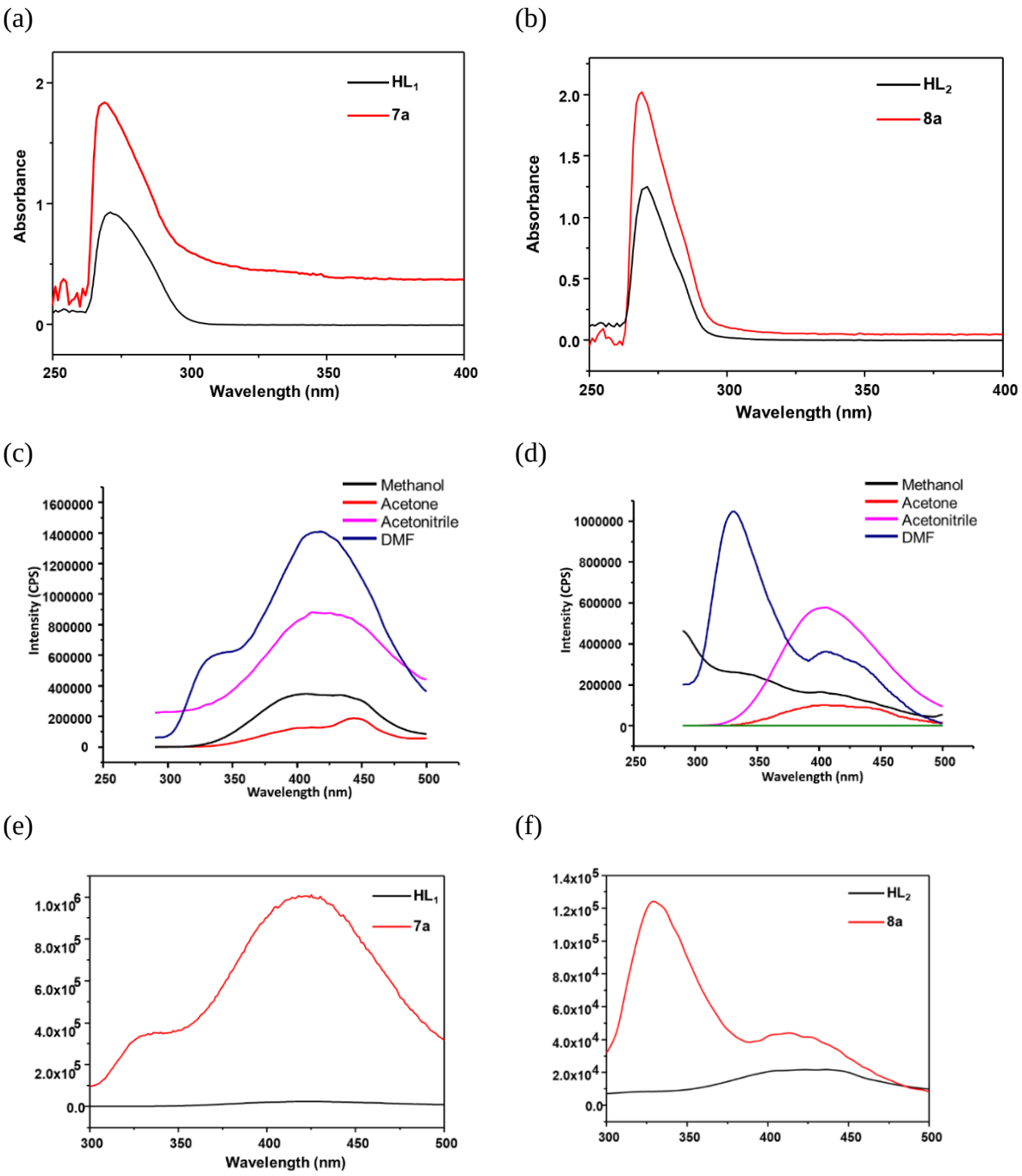

Fig. S10. (a) UV-Vis spectra of constituting ligands of **CSMCRI-7**, and **7a** (b) UV-Vis spectra of constituting ligands of **CSMCRI-8**, and **8a**. (c) Luminescence spectra of **7a** in different solvents (d) Luminescence spectra of **8a** in different solvents. (e) Luminescence spectra of **7a** and H***L1*** in DMF (f) Luminescence spectra of **8a** and H***L2*** in DMF.

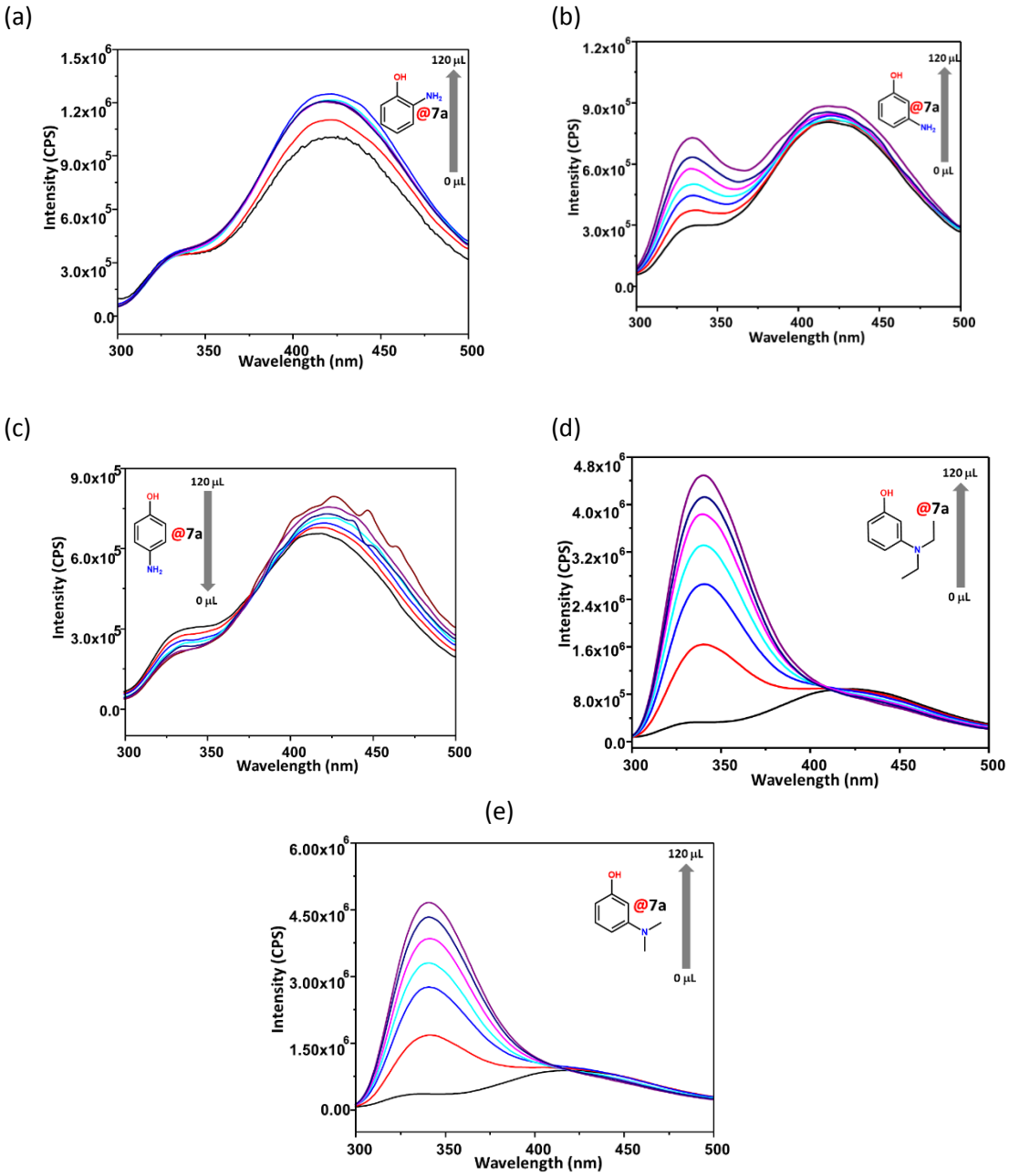

Fig. S11. Emission spectra of **7a** upon incremental addition of aminophenol solutions (1 mM) (a) 2-AP, (b) 3-AP, (c) 4-AP, (d) DEP, and (e) DMP in DMF.

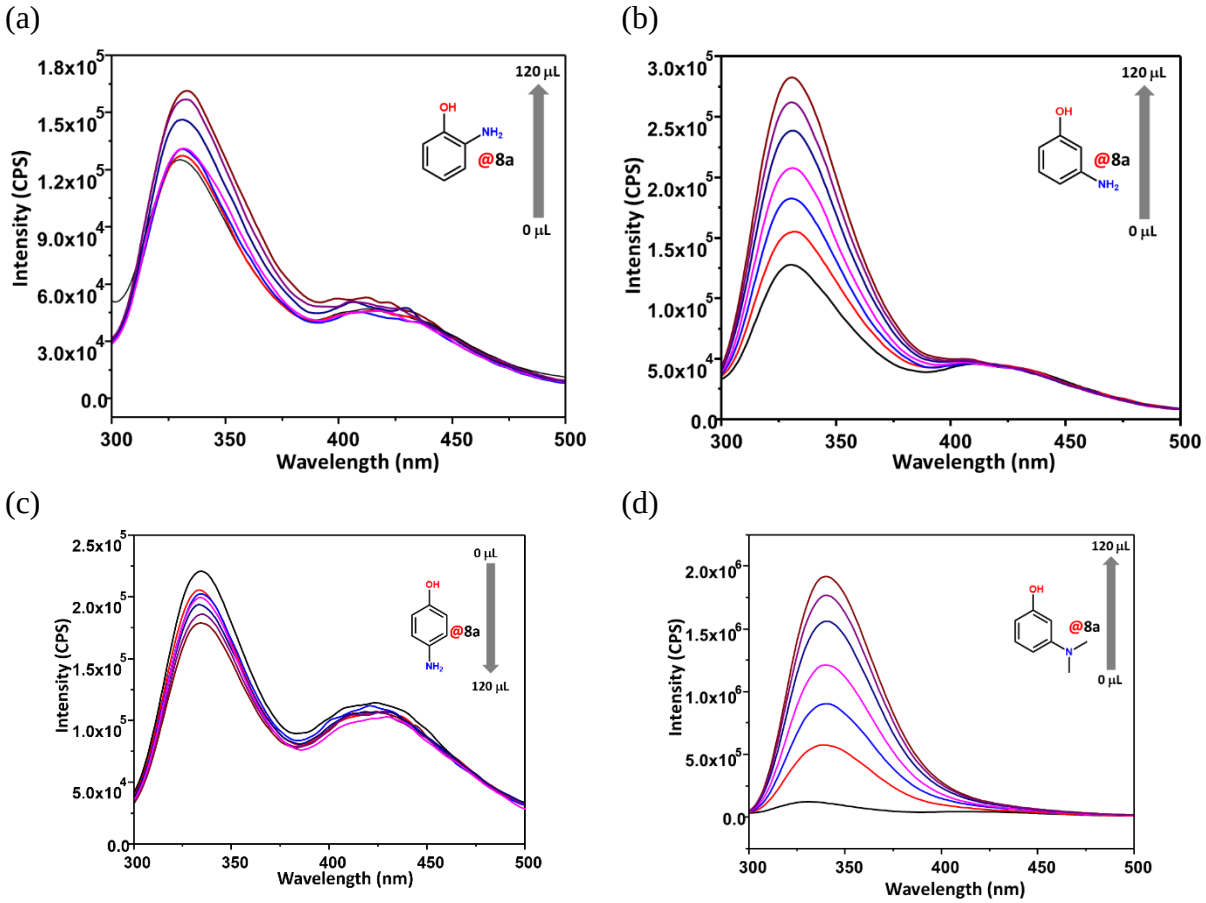

Fig. S12. Emission spectra of **8a** upon incremental addition of aminophenol solutions (1 mM) (a) 2-AP, (b) 3-AP, (c) 4-AP, and (d) DMP in DMF.

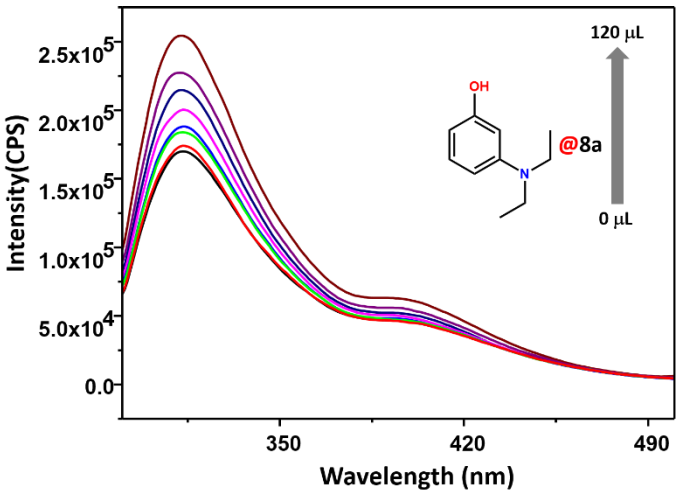

Fig. S13. Emission spectra of **8a** upon incremental addition of DEP solution (10 µM) in DMF.

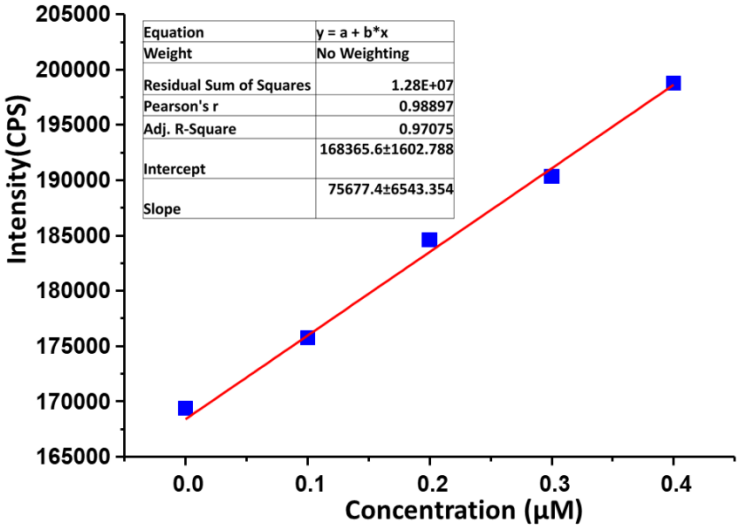

Fig. S14. Linear region of fluorescence intensity of **8a** upon addition of DEP (0 – 120 μL, 10 μM stock solution).

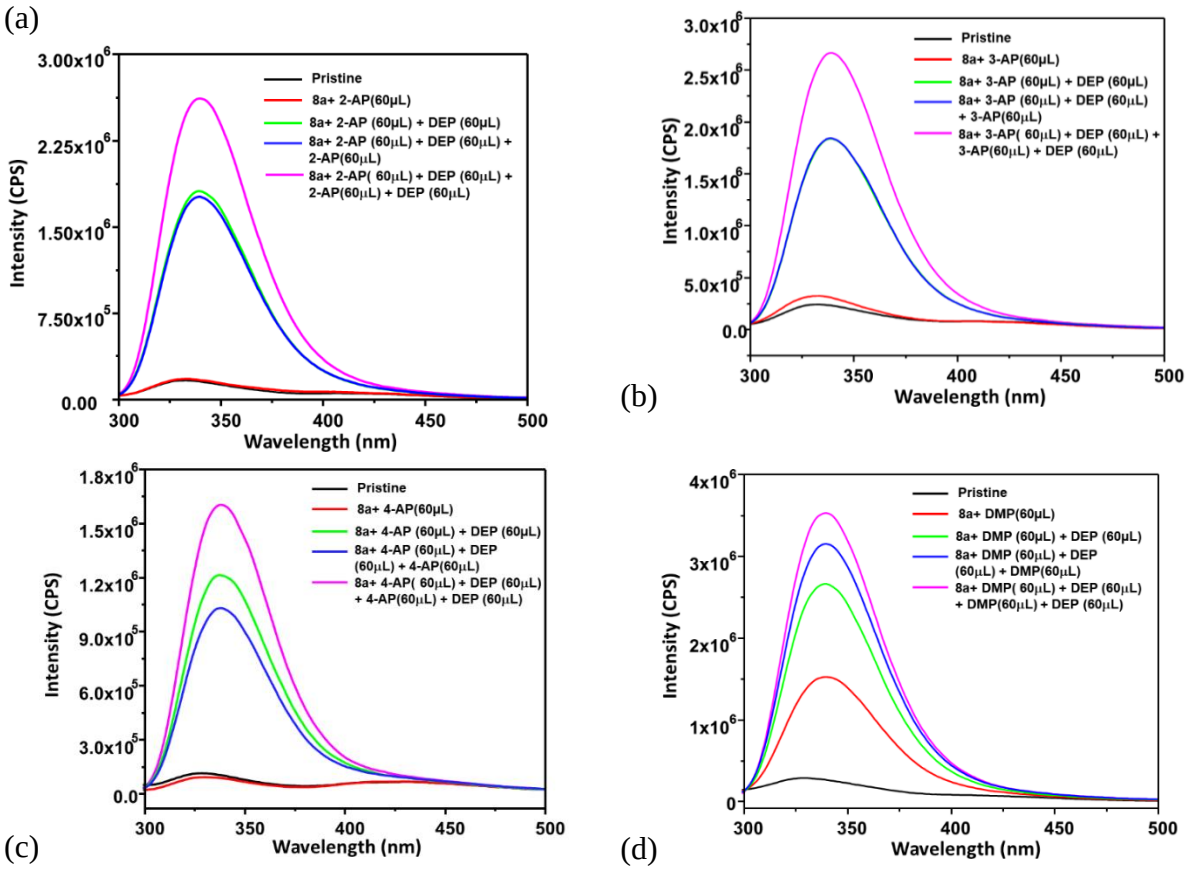

Fig. S15. Change in fluorescence spectrum of **8a**, upon addition of DEP in presence of (a)2-AP, (b) 3-AP, (c) 4-AP, and (d) DMP**.**

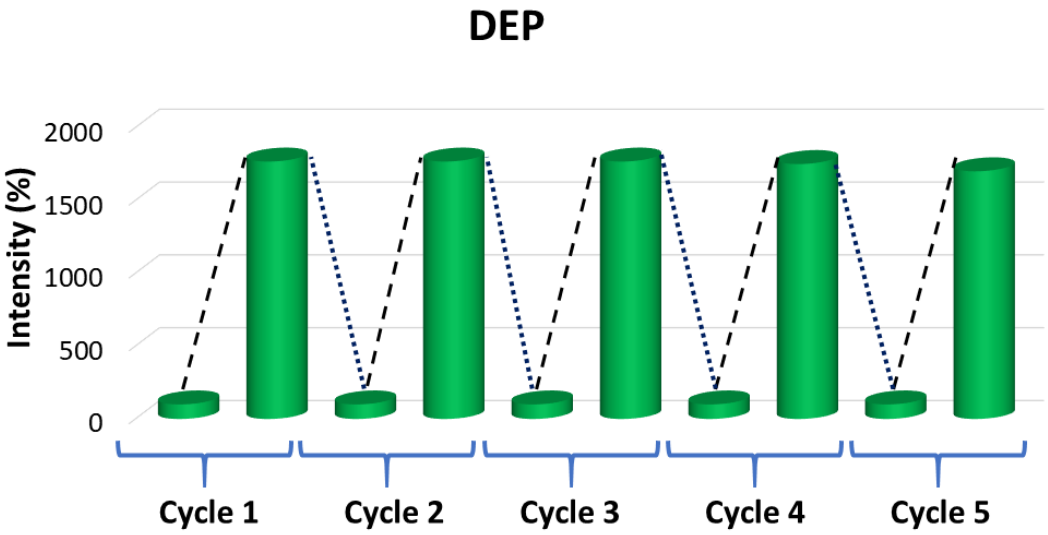

Fig. S16. Reproducibility of enhancement efficiency of **8a** up to five cycles, toward 120 µL (1 mM) addition of DEP solution in DMF.

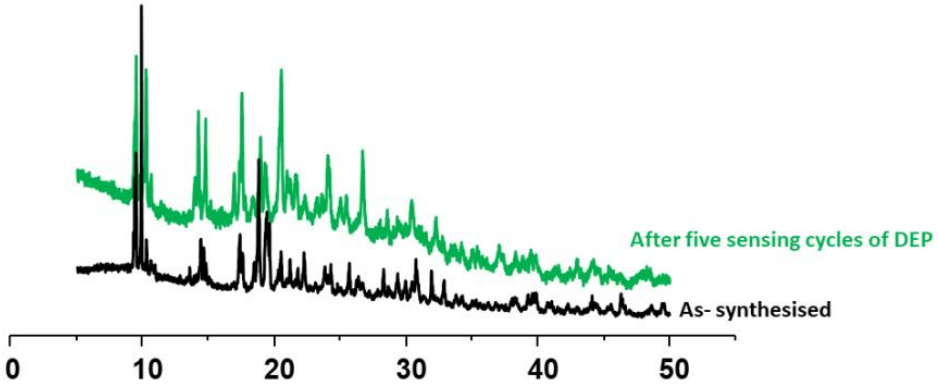

Fig. S17. PXRD curves of **8a** after five sensing recovery cycles for IPT (5 mM), showing that structural integrity of the framework is maintained.

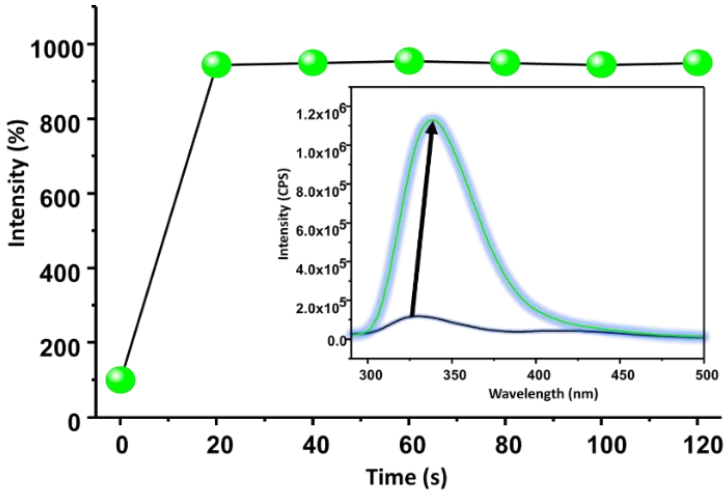

Fig. S18. Change in fluorescence intensity of **8a** in the time span of 120 s upon additions of 40 µL (1 mM) of DEP (in DMF) (inset shows a rapid change within initial 20 s).

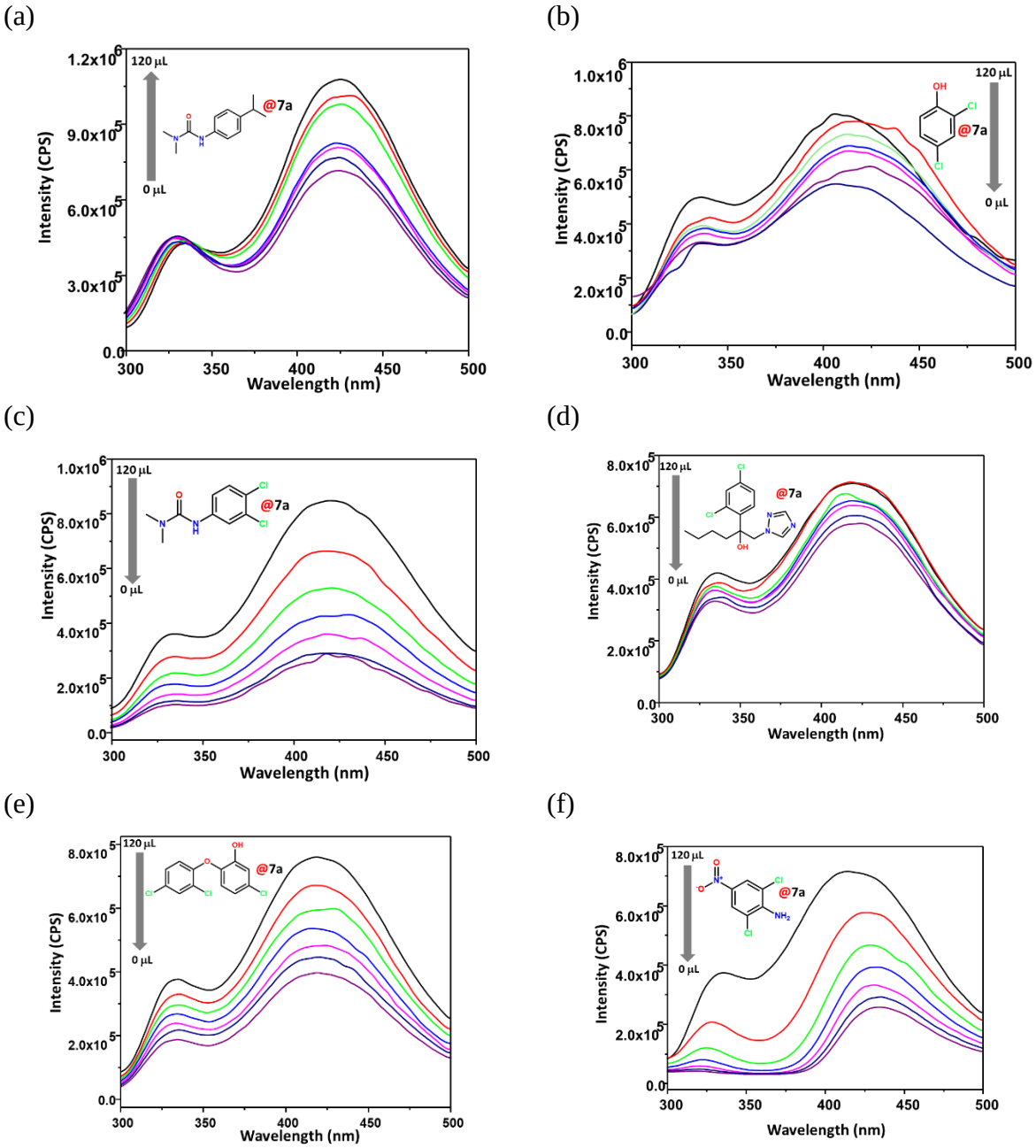

Fig. S19. Emission spectra of **7a** upon incremental addition of solution (5 mM) of (a) IPT, (b) DCP, (c) DUN, (d) HCL, (e) TCHDE and (f) DCNA in DMF.

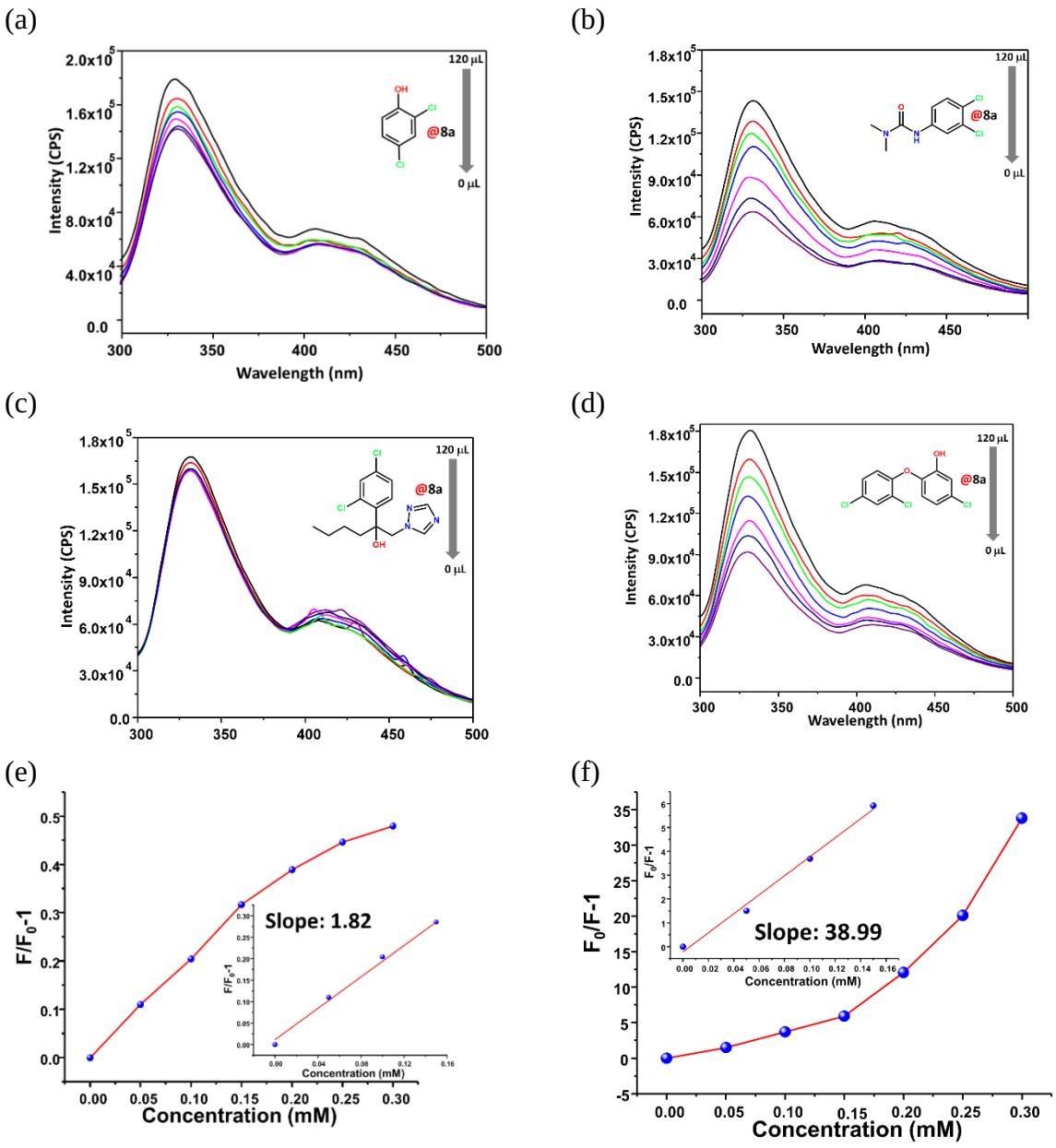

Fig. S20. Emission spectra of **8a** upon incremental addition of solution (5 mM) of (a) DCP, (b) DUN, (c) HCL, and (d) TCHDE in DMF. **S**-V plot for 8a upon incremental addition of (e) IPT and (f) DCNA (inset displays the straight region of the S-V plot)

(a) (b)

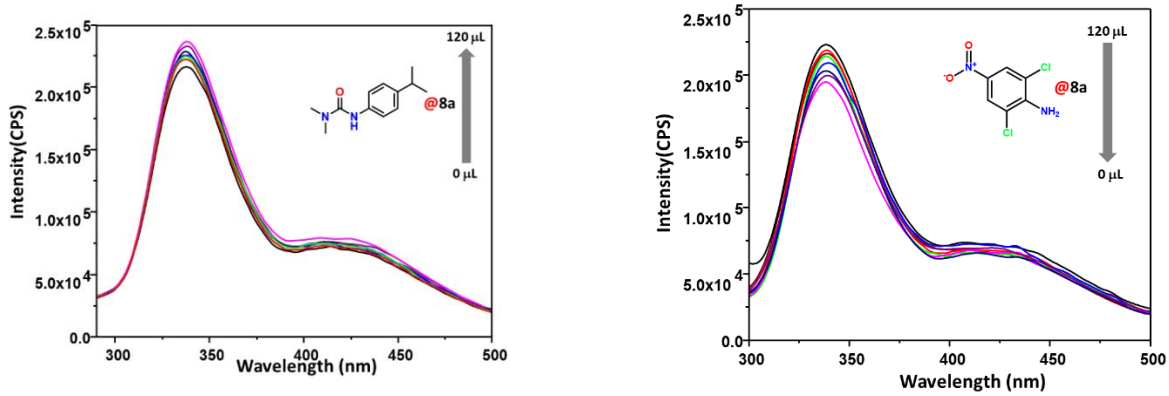

Fig. S21. Emission spectra of **8a** upon incremental addition of IPT (a) and DCNA (b) solution (10 µM) in DMF.

(a) **(b)**

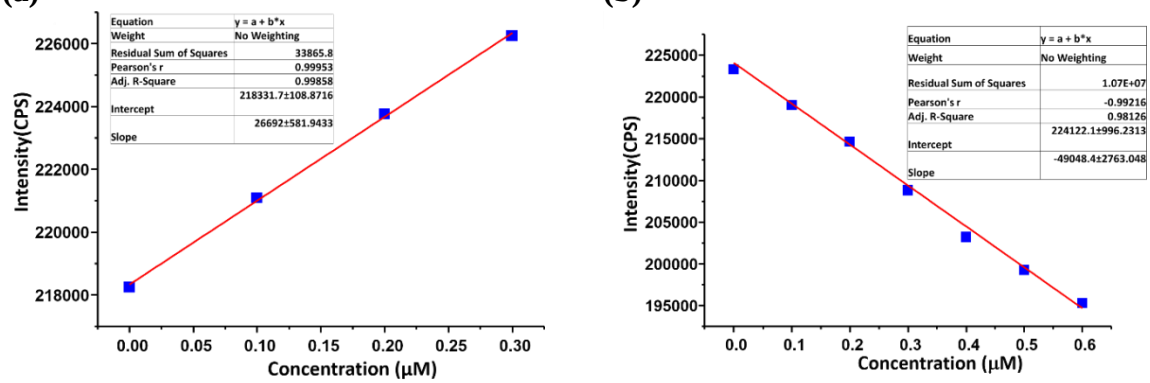

Fig. S22. Linear region of fluorescence intensity of **8a** upon addition of IPT and DCNA (0 – 120 µL, 10 µM stock solution).

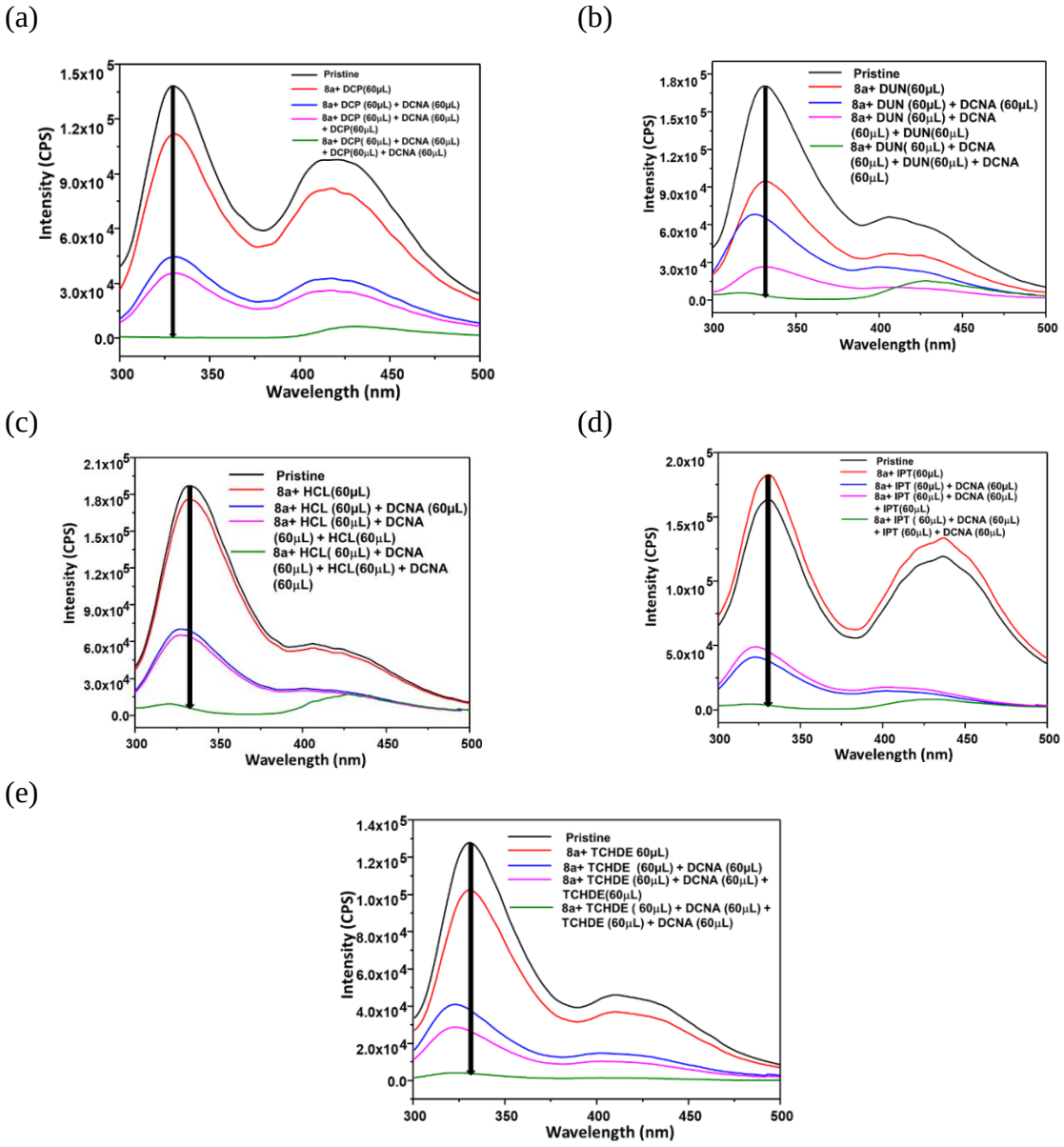

Fig. S23. Change in fluorescence spectrum of **8a**, upon addition of DCNA in presence of (a) DCP, (b) DUN, (c) HCL, (d) IPT and (e) TCHDE.

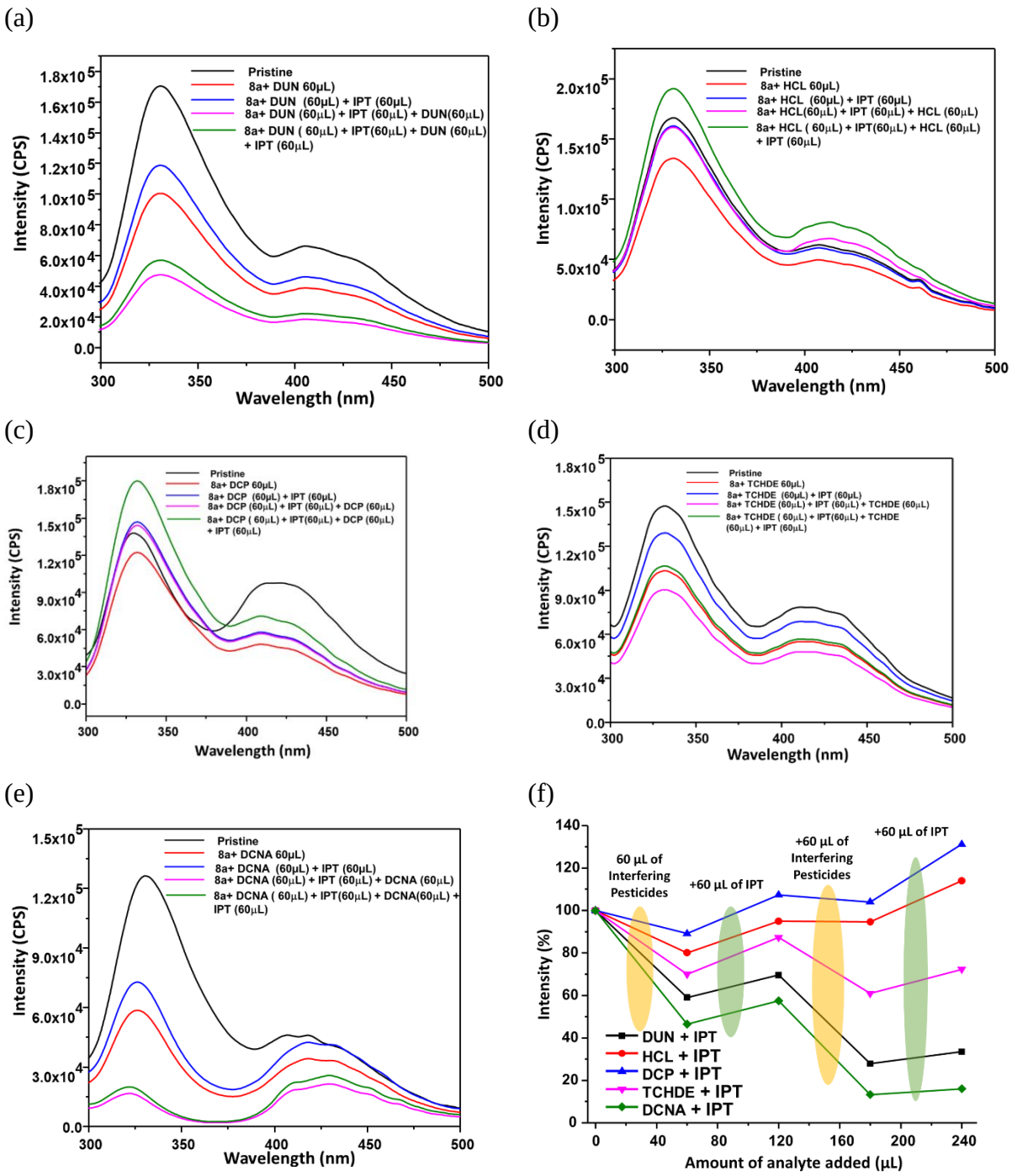

Fig. S24. Change in fluorescence spectrum of **8a**, upon addition of IPT in presence of (a) DUN, (b) HCL, (c) DCP , (d) TCHDE and (e) DCNA**.** (f) Interference plot for change in PL intensities upon addition of different pesticides (120 μL, 5 mM), followed by IPT.

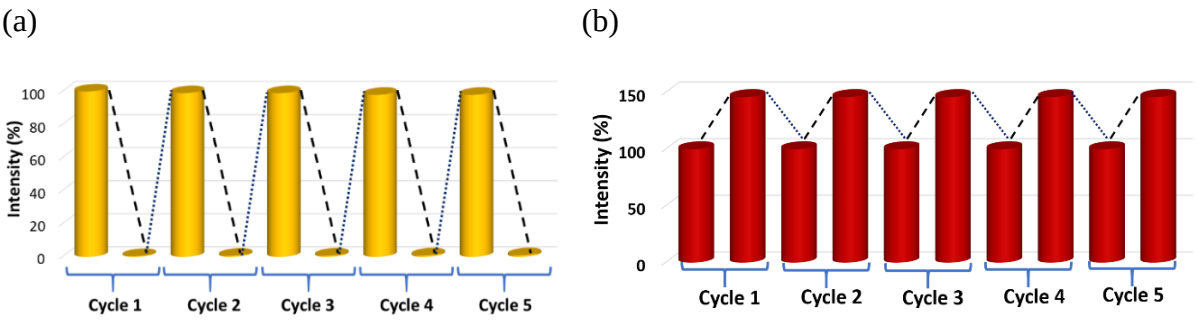

Fig. S25. Reproducibility of enhancement efficiency of **8a** up to five cycles, toward 120 µL (5 mM) addition of (a) DCNA and (b) IPT solution in DMF.

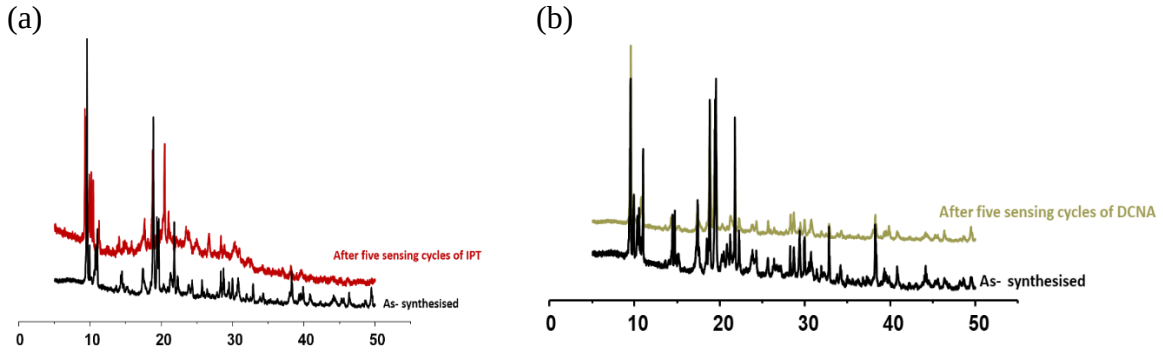

Fig. S26. PXRD curves of **8a** after five sensing recovery cycles for (a) IPT (5 mM) & (b) DCNA (5 mM), showing that structural integrity of the framework is maintained.

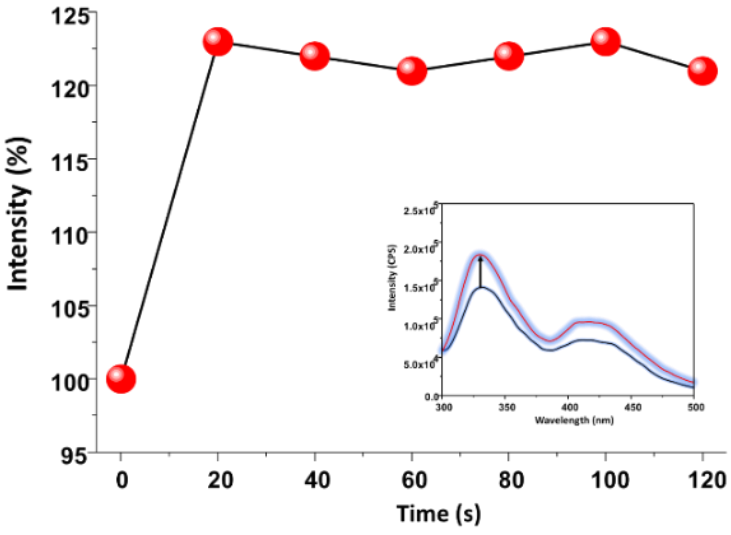

Fig. S27. Change in fluorescence intensity of **8a** in the time span of 120 s upon additions of 40 µL (5 mM) of IPT (in DMF) (inset shows a rapid change within initial 20 s).

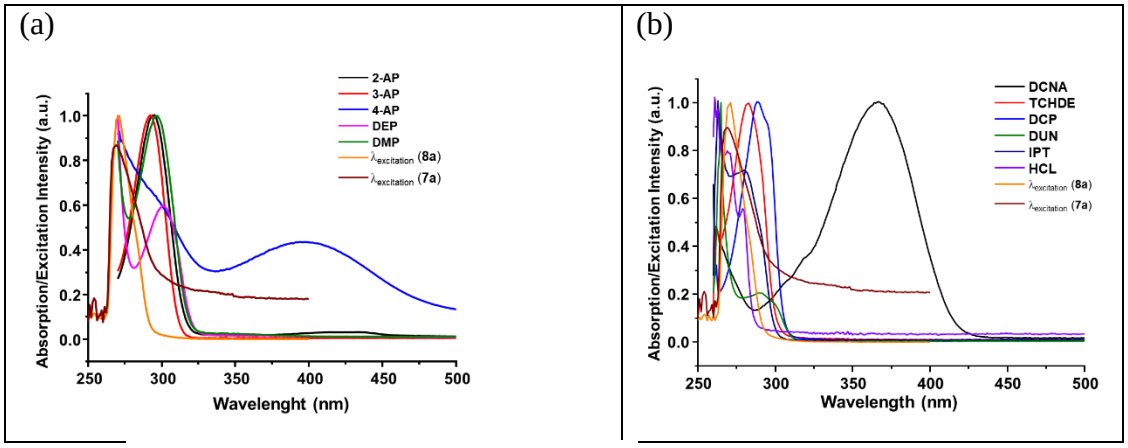

Figure S28. Overlap between absorbance spectra of aminophenols (a) and pesticides (b) with excitation spectra of 7a and 8a.

Microscopic Models for the MOF Surface: ([001] Surface)

The optimized bulk structures, i.e. super cell structure from 4-unit cells (1 × 4 ×1), of both isostructural **7a** and **8a** was used to identify the sets of Miller indices that would result in a favourable surface, via the Bravais–Friedel–Donnay–Harker method.[22,23] Out of the so-selected Miller indices, the [001] surface was selected for both **7a** and **8a**, since this surface expose the pores to interact guest analytes directly with inorganic part of MOF and effective interactions with the organic linker and analyte, are thus relevant for adsorption and separation applications. A visual inspection and comparison of the faces identified revealed that [001] hkl values gave suitable adsorption of guest to **7a** and **8a**. Therefore, the calculations were performed using the [001] face, as this was the one most likely to dominate the crystal habit. The planes considered for these cuts are shown in Fig. S29. Both **7a** [001] surface and **8a** [001] surface was modeled by a (1 × 1) slab with 10.0 Å depth from the optimized **8a** single crystal. Model of **7a** [001] surface was built considering slab depths of 10 Å of the bulk crystal and the (1 × 1) slab model of around 16.839 and 38.273 Å. Further, the [001] surfaces were constructed considering 3D periodic boundary conditions, and their dimensions were of 16.839 and 38.273 Å for *a* and *c*, respectively and depth of 34.036 Å along the *b* direction (the direction perpendicular to the surface slabs) for **7a** (Fig. S29a). A vacuum layer was inserted along the *b* direction, with a thickness greater than 10 Å, in order to decouple the interactions between periodic images. The net dipole driven by the surface cleavage was eliminated by translating some of the organic linkers from the top to the bottom of the facets. In order to cure the dangling bonds, the organic carbons and carboxylate oxygen were capped with hydrogen atoms. The **8a** [001] surface containing altogether 16 Cd, 402 C, 248 H, 78 N and 80 O atoms, and a 10 Å thick vacuum layer above the slab. In a similar manner the **8a** [001] surface model was also built with dimensions of 16.836 and 38.169 Å for *a* and *c*, respectively and depth of 34.036 Å along the *b* direction (Fig. S29c) with composition of 16 Cd, 360 C, 240 H, 120 N and 80 O atoms, and a 10 Å thick vacuum layer above the slab. The final surface models were then geometry-optimized using the Quickstep module of the CP2K package[9] and considering the same level of theory and parameters as for the optimization of the bulk model. All the atomic coordinates of the surface models were relaxed and all the calculations were performed at the Γ-point. The final DFT-geometry-optimized **7a** and **8a** slab model was used to provide a suitable contact surface with the

analytes (e.g. DCNA, DEP, IPT). Subsequently, the analytes loaded **7a** and **8a** surface [001] was also geometry optimized with the same level of theory. Finally, the geometry optimized **8a** surface [001] without (Fig. S29b and S29d) and with analytes (Fig. S30) were used to explore the single point energy and further extraction of HOMO and LUMO energy (for understanding the optical properties) of the pesticide loaded MOF with the same level of theory and parameters as for the optimization of the **8a** surface [001] model.

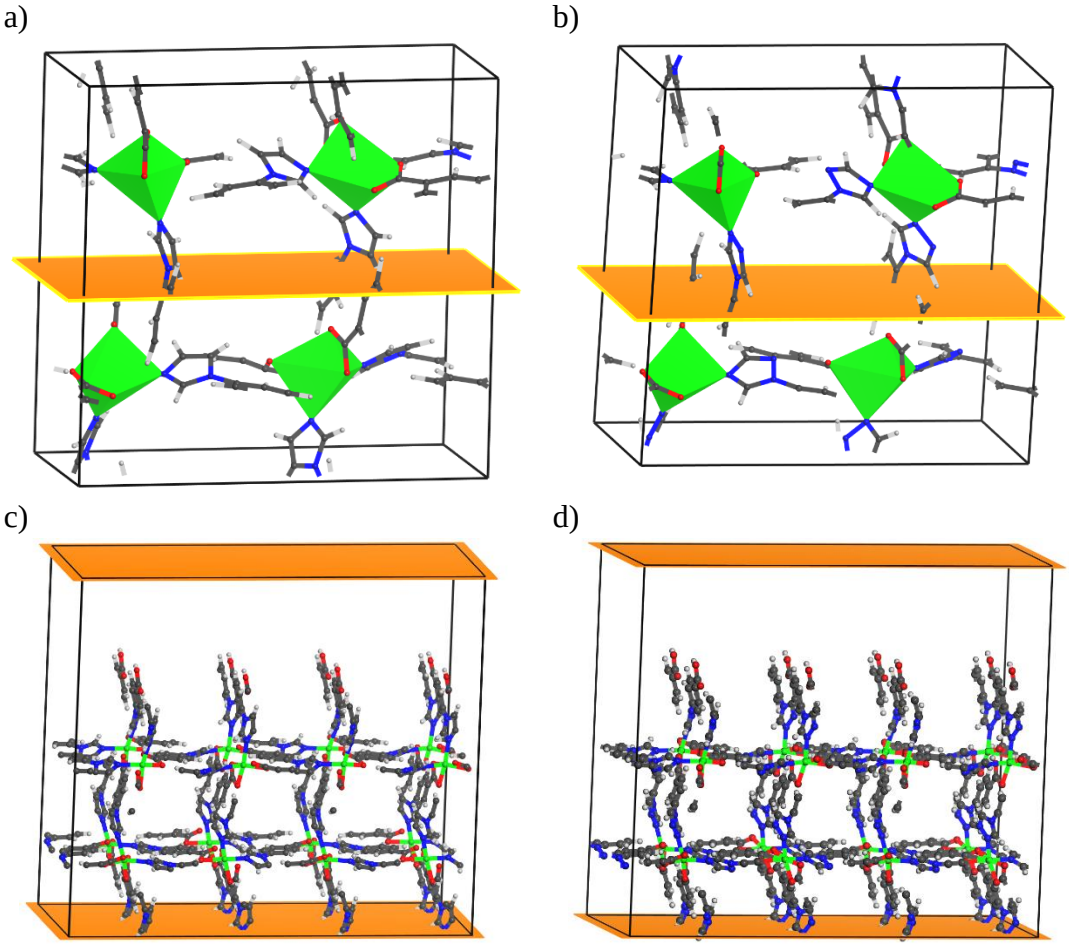

Fig. S29. (a) The unit cell of viewed along b direction with slight tilting to view properly exposing the [001] miller plane (solid orange planes) of DFT optimized **7a** (a) and **8a** (b). The slab cut exposing the [001] miller plane of **7a** (c) and **8a** (d) showing the orientations along b direction. (Gray, carbon; blue, nitrogen; white, hydrogen; red, oxygen; green, cadmium).

a)

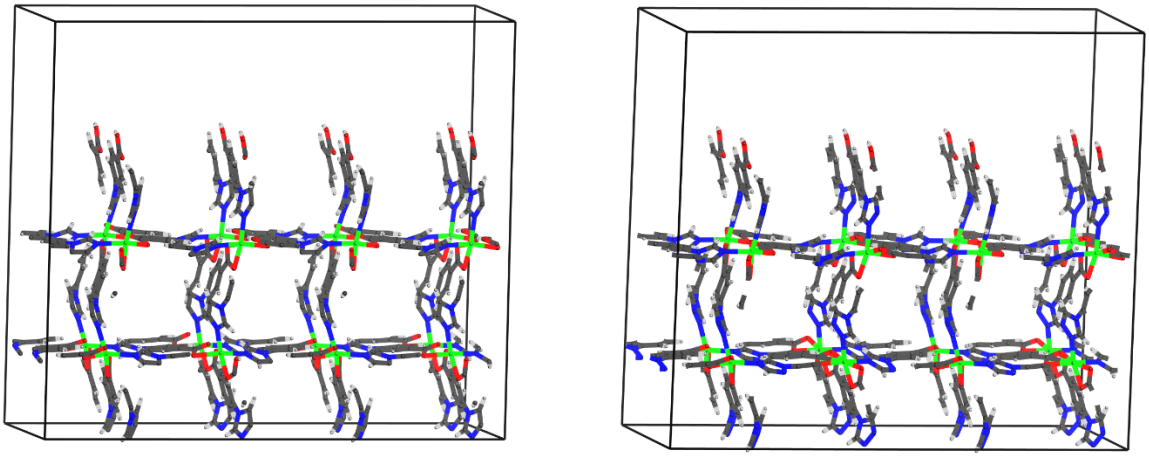

b)

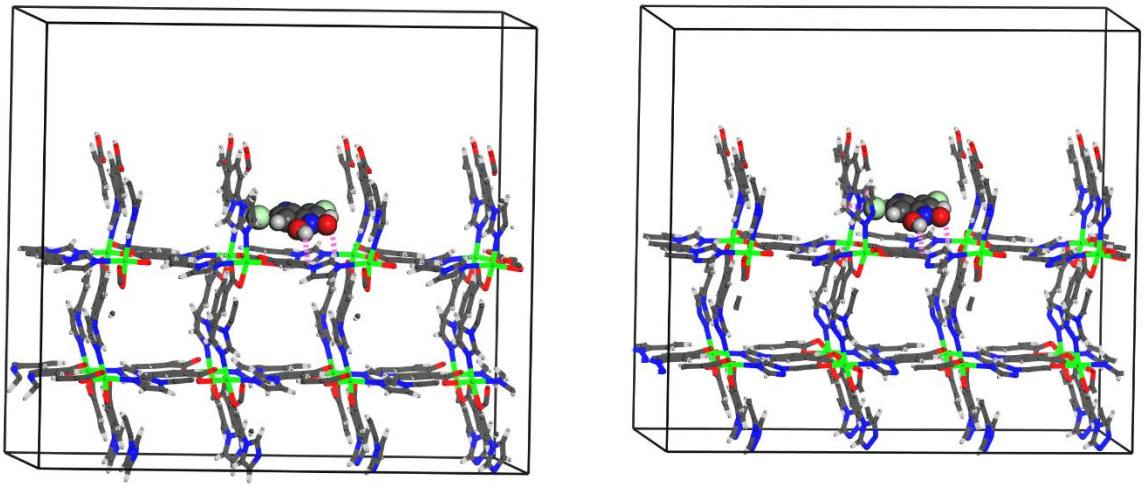

c)

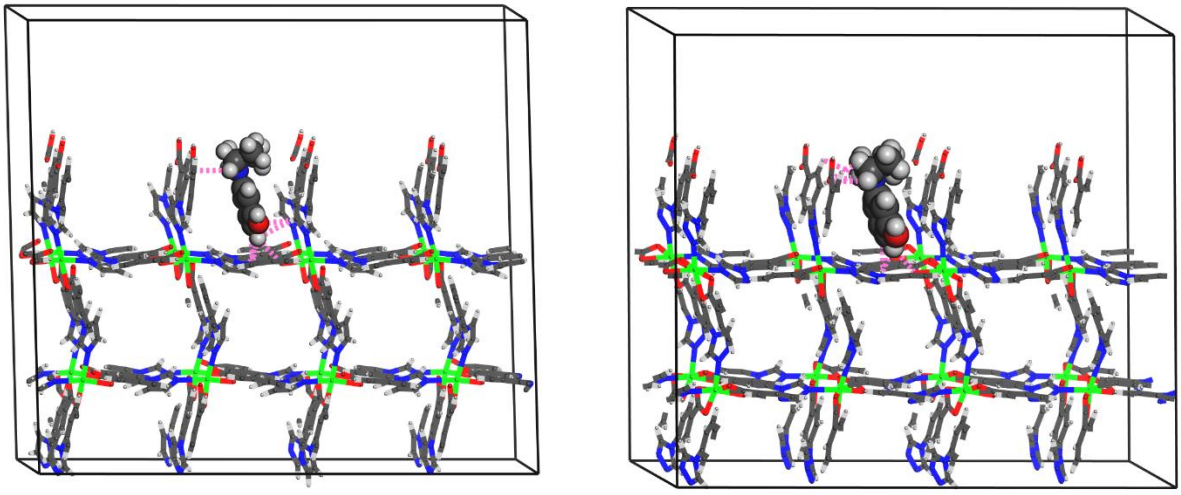

d)

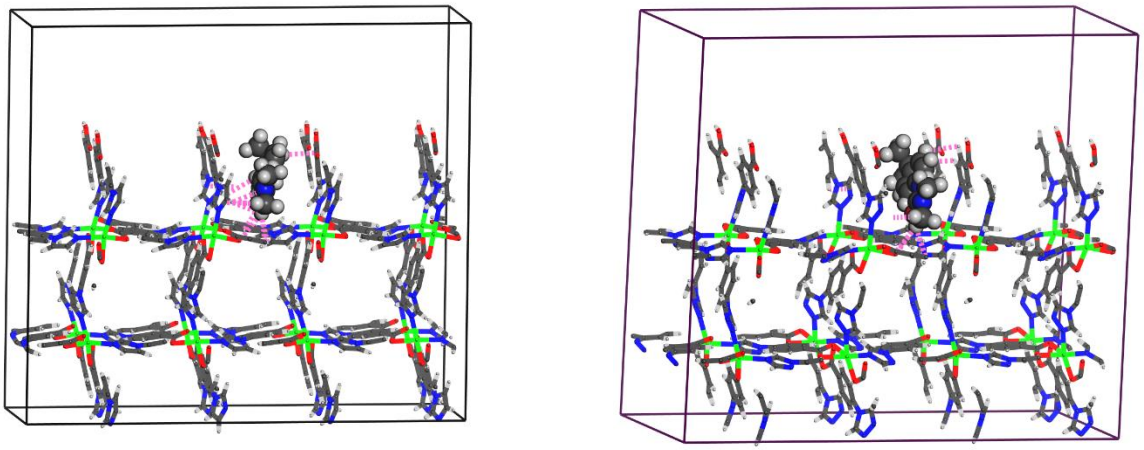

Figure S30. DFT-optimized **7a** [101] surface (left) and **8a** [101] surface (a) with analytes, DCNA (b), DEP (c) and IPT (d) viewed along *b* direction. (Gray, carbon; blue, nitrogen; white, hydrogen; red, oxygen; green, cadmium, Chlorine; green, and hydrogen bonding network represent in dotted cyan line).

6. Microscopic Models for the Analytes

All experimentally investigated analytes, i.e DCNA, DEP, IDP, were then geometry-optimized using the Quickstep module of the CP2K package[9] and considering the same level of theory and parameters as for the case of **8a** [101] surface. In order to keep the identical plane wave cut off for all calculations, the same periodic boundary conditions of **8a** surface [101] were also used for the geometry optimizations of all analytes, each molecule was placed at the centre of the simulation box with dimensions as similar to the slab models, i.e. 16.663, 34.370 and 37.974 Å. Fig. S31 represents all the DFT-optimized analytes, i.e. DCNA, DEP, IDP etc. Then, the geometry optimized analytes were used to explore the single point energy and further extraction of HOMO and LUMO energy.

(a)

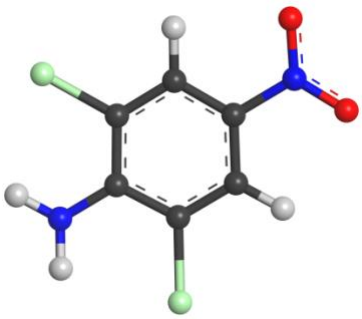

(b)

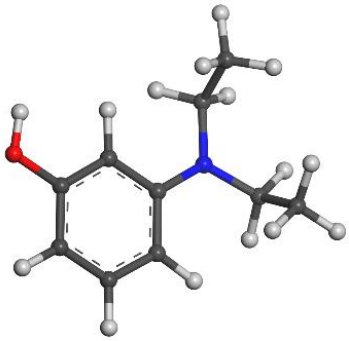

(c)

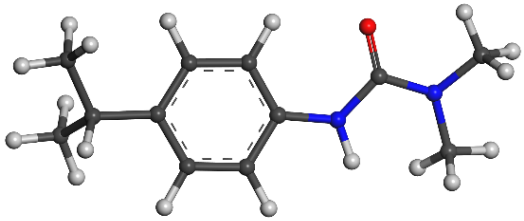

Fig. S31. DFT optimized structures of studied analytes: (a) DCNA, (b) DEP and (c) IPT.

Table S4. Crystal data and structure refinement for **CSMCRI-7** and **CSMCRI-8**

Identification code	**CSMCRI-7**	**CSMCRI-8**
Empirical formula	$C_{26}H_{28}CdN_6O_6$	$C_{24}H_{26}CdN_8O_6$
Formula weight	632.96	634.94
Temperature/K	173.15	273.15
Crystal system	orthorhombic	orthorhombic
Space group	*Pc2₁b*	*Pca2₁*
a/Å	8.214(4)	18.8515(19)
b/Å	17.985(9)	8.2335(8)
c/Å	18.935(9)	18.1781(18)
α/°	90	90
β/°	90	90
γ/°	90	90
Volume/Å^3	2797(2)	2821.5(5)
Z	4	4
ρ_{calc}g/cm^3	1.5030	1.4946
μ/mm^{-1}	0.831	0.826
F(000)	1285.3	1285.3
Crystal size/mm^3	0.12 × 0.1 × 0.08	0.22 × 0.18 × 0.18
Radiation	Mo Kα (λ = 0.71073)	Mo Kα (λ = 0.71073)
2Θ range for data collection/°	4.32 to 56.72	4.32 to 56.72
Index ranges	-9 ≤ h ≤ 8, -21 ≤ k ≤ 20, -22 ≤ l ≤ 20	-24 ≤ h ≤ 21, -10 ≤ k ≤ 5, -20 ≤ l ≤ 23
Reflections collected	13900	13505
Independent reflections	4937 [R_{int} = 0.0256, R_{sigma} = 0.0332]	5830 [R_{int} = 0.0283, R_{sigma} = 0.0391]
Data/restraints/parameters	4937/1/353	5830/1/357
Goodness-of-fit on F^2	1.041	1.057
Final R indexes [I>=2σ (I)]	R_1 = 0.0275, wR_2 = 0.0666	R_1 = 0.0395, wR_2 = 0.0911
Final R indexes [all data]	R_1 = 0.0307, wR_2 = 0.0682	R_1 = 0.0488, wR_2 = 0.0985
Largest diff. peak/hole / e Å^{-3}	0.85/-0.27	0.73/-0.57

Table S5. Calculation of standard deviation of fluorescence intensity and limit of Detection for **8a** towards DEP

Blank Reading (**8a**)	Fluorescence Intensity (CPS)
Reading 1	219856
Reading 2	221959
Reading 3	217692
Reading 4	220085
Reading 5	222871
Standard Deviation(σ)	2013.819332
The slop of the graph(K)	75677 μM^{-1}
Detection Limit(3σ/K)	0.0798 μM
Limit of detection (DEP)	0.039 ppm
Limit of detection (DEP)	79.8 nM

Table S6. Calculation of standard deviation of fluorescence intensity and limit of detection for **8a** towards IPT

Blank Reading (**8a**)	Fluorescence Intensity (CPS)
Reading 1	219856
Reading 2	221959
Reading 3	217692
Reading 4	220085
Reading 5	222871
Standard Deviation(σ)	2013.819332
The slop of the graph(K)	26692 μM^{-1}
Detection Limit(3σ/K)	0.226 μM
Limit of detection (IPT)	0.110 ppm
Limit of detection (IPT)	226 nM

Table S7. Calculation of standard deviation of fluorescence intensity and limit of detection for **8a** towards DCNA

Blank Reading (**8a**)	Fluorescence Intensity (CPS)
Reading 1	219856
Reading 2	221959
Reading 3	217692
Reading 4	220085
Reading 5	222871
Standard Deviation(σ)	2013.819332
The slop of the graph(K)	49048 μM^{-1}
Detection Limit(3σ/K)	0.124 μM
Limit of detection (DCNA)	0.060 ppm
Limit of detection (DCNA)	124 nM

Table S8. Low pressure (1bar) CO_2 adsorption capacities in Metal-Organic Frameworks at 273K

S.No.	Chemical formula	Common name	BET (m^2/g)	Capacity (cm^3/g)	- *Qst* kJmol^{-1}	*Ref.*
1.	$Er_2(PDA)_3$	-	-	11.71	30	*J. Am. Chem. Soc.*, ***2003***, *125, 10, 3062-3067*
2.	$[Cd(bpydc)_2(DMF)_2{\cdot}2DMF]_n$ (JMS-3)	JMS-3a		30.89	34.4	*Front Chem.*, **2020**, 8, 581226
	$[Zn(bpydc)(DMF){\cdot}DMF]_n$ (JMS-4)	JMS-4a		16.08	30.7	
3.	$[Co^{II}_4(\mu\text{-}OH_2)_4(MTB)_2{\cdot}(H_2O)_4]_n$ $\cdot 13n$DMF$\cdot 11n H_2O$	SNU-15	356	35.7	-	*Chem. Commun*,. **2009**, *2296–2298*
4.	$CuB(4\text{-}MIm)_4$	BIF-8-Cu	1287	34.1		*J. Am. Chem. Soc.*, **2009**,131,17, *6111-6113*
	$LiB(4\text{-}MIm)_4$	BIF-9-Li	1523	35.6	-	
5.	--	Cu-NTTA	3931	115.6	-	*ACS Appl. Mater. Interfaces*, **2017**, *9*, 26177−26183
6.	-	UiO-66-1,4-Naphthyl	757	7.12	25.8	*Langmuir*, **2012**, *28*, 15606−15613
7.	$Cu_2(2\text{-}MeBPDC)_2(DMA)_2$	MOF-602	910*	25.45		*J. Am. Chem. Soc.*, **2008**, *130*, 35, 11650-11661
	$Cu_2(IBPDC)_2(Py)_{1.67}(H_2O)_{0.33}$	MOF-603	460*	25.45	-	
8.	-	UiO-66(Zr)-$(SH)_2$	308	5.6		*Angew. Chem., Int. Ed.*, **2015**, *54*, 5142–5146
9.	$[Zn(hfipbb)(bpt)]_n{\cdot}n(DMF)_2{\cdot}n(H_2O)$ (1)		-	21.4	33.6	*Cryst. Growth Des.* **2018**, *18*, 7570−7578
10.	UiO-66(Hf)-$(COOH)_2$		378	6.1	28.2	*Inorg. Chem.*, **2016**, *55, 3*, 1134-1141
	UiO-66(Hf)-$(F)_4$		329	4.17	23.2	
11.	UiO-66(Zr)-$(OCH_2CH_3)_2$		405	3.31	26.2	*Inorg. Chem.*, **2015**, *54*, 4862−4868
	UiO-66(Zr)-$(F)_4$		833	6.21	18.7	
	UiO-66(Zr)-$(COOH)_4$		212	2.70	30.5	
12.		NUM-3a	2111	112.89	24.1	*J. Am. Chem. Soc.*, **2009**,*131,17*, 6111-6113
13.	$[Cu_2(BDPT^{4-})(H_2O)_2]$	HNUST-1	1400	156.29	31.2	*CrystEngComm*,, **2013**, *15*, 3517-3520
14.	$[CuL_2(NO_3)_2$□o-xylene DMF$]_n$	1□NO_3^-		84	-	*Chem. Eur. J.*, **2015**, *21*, 7071–7076
15.	$[Cu_2PDAI(H_2O)]$	PCN-124	1372	145.6	26.3	*Chem. Commun., 2012,48, 9995-9997*
16.	$Al_4(OH)_2(OCH_3)_4(BDC\text{-}NH_2)_3$	CAU-1	1268	122.69	48	*Energy Environ. Sci.*, **2011**,*4*, 4522-4527
17.	$\{[Zn_2(TPOM)(3,7\text{-}DBTDC)_2]{\cdot}7H_2O{\cdot}DMA\}_n$ (1)	1	28.2		34.1	*ACS Appl. Mater. Interfaces*, **2020**, *12*, 11724−11736
	$\{[Cd_2(TPOM)(3,7\text{-}DBTDC)_2]{\cdot}6H_2O{\cdot}3DMF\}_n$ (2).	2	37.8		31.7	
18.	$Co_4(OH)_2(p\text{-}CDC)_3$	-	1080	83.49	-	*Small*, **2009**, *15*, 1727-1731

19.	$(Me_2NH_2)_{1.75}[In(L)]_{1.75}(DMF)_{12}(H_2O)_{10}$	NOTT 202a		-	22	*Nat. Mater.*, **2012**, *11*, 710-716
20.	$[\{Zn(BINDI)_{0.5}(bpa)_{0.5}(H_2O)\}.4H_2O]_n$	MOF1	84	22.8	33.8	*Inorg. Chem. Front.*, **2019**, *6*, 1058-1067
	$[\{Zn(BINDI)_{0.5}(bpe)\}.3H_2O]_n$	MOF2	30	12.1	34.2	
21.	$[Zn(btz)]\cdot DMF\cdot 0.5H_2O\}_n$ (H_2btz = 1,5-bis(5-tetrazolo)-3-oxapentane	Zn-btz	1151	181.24	31.2	*J. Am. Chem. Soc.*, ***2012***, *134*, 18892-18895
22.	$\{[Cu_2(4\text{-TPOM})(3,7\text{-DBTDC})_2]\cdot 4H_2O\cdot 3DMF\}_n$ (1)	-	385**	63	-	*Inorg. Chem.*, **2021**, *60*, 5071−5080
23.	$\{[Cu\text{-}(MTABA)(H_2O)]\cdot 4H_2O\cdot 2EtOH\cdot DMF\}_n$	Cu-MOF(1)	349.2**	45.58		*ACS Appl. Mater. Interfaces*, **2020**, *12*, 37137−37146
24.	$\{[Zn(SDB)(3,3'\text{-}L)_{0.5}]\cdot xG\}_n$	IITKGP-13A	206	45.02	25	*Inorg. Chem.*, **2020**, *59*, *10*, 7056–7066
	$\{[Zn_2(SDB)_2(4,4'\text{-}L)]\cdot xG\}_n$	IITKGP-13B	129	18.59	-	
25.	$Zn(5\text{-mtz})_2$·guest (5-Hmtz 5-methyltetrazole)	TTF-4	1172	67.71	16.7	*Chem. Commun.*, **2016**,*52*, 5625-5628
26.	$Cu_2(BPnDC)_2(bpy)$	SNU-6	2590	50.4	-	*Chem.—Eur. J.*, **2008,** *14*, 8812-8821
27.	rht-MOF-1		2100	90.11	28.5	*Chem. Commun.*, ***2015***,*51*, 9636-9639
28.	$[Cu_2(PDAD)(H_2O)]_n$	PCN-124-stu	2153	159.85	26	*Chem. Eur. J.*, **2017**, *23*,13058–13066
29.		UMCM-1		-	12	*J. Phys. Chem. C*, **2010,** *114*, *14*, 6464-6471
30.		MOF-5	3200*	-	16.5	*Microporous Mesoporous Mater.*, **2008**, *116*, 727–731
31.		IRMOF-1	1100	-	14	*Langmuir*, **2009**, *25*, *13*, 7383-7388
		IRMOF-3	630	-	19	
		HKUST-1	1540	-	14.6	
32.	$\{[Zn(CHDC)(L)].H_2O\}_n$ (1)	--	7	4		*Chem. Eur.J.*, **2018**, *24*,15831 –15839
	$\{[Cd(CHDC)(L)].H_2O\}_n$ (2)		19	6		
33.		NU-1000	2320	-	17	*J. Am. Chem. Soc.*, **2013**, *13545*, 16801-16804
34.	$\{[Zn_5(dmtrz)_3(IPA)_3(OH)]\cdot DMF\cdot H_2O\}_n$	MAC-4	796	34.2	21	*Dalton Trans.*, **2012**, *41*, 4007–4011
	$\{[Zn_5(dmtrz)_3(OH\text{-}IPA)_3(OH)]\cdot DMF\cdot 5H_2O\}n$	MAC-4-OH	339	69.3	31	
35.	$[Zn_2Ca(bdc)_3(H_2O)_2]_n$•x(solvent)		586	75.1	27.8	*Inorg. Chem. Commun.*, **2020**, *121*, 108202
36.	$\{[Co(BDC)(L)\cdot 2H_2O]\cdot xG\}_n$	CoMOF-2	6.8	51	35	*Inorg. Chem.* **2019**, *58*, 10084−10096
37.	$[Cu(BDC\text{-}NO_2)(DMF)]\cdot x$Solvents	$CuBDC\text{-}NO_2\text{-}a$	523	73.92	20.2	*Inorg. Chem.* **2020**, *59*, *23*, 17143–17148
38.	**7a**	**7a**	18	28.29	24.02	***Present Work***
	8a	**8a**	23	53.65	22.08	

*****Langmuir Surface Area

****** Based on CO_2 adsorption data@195K

Table S9. A comparison of quenching constant, their LOD values, of various luminescent MOFs used for detection of DCNA.

S. No.	LMOF/ Coordination Polymer	Quenching constant (M^{-1})	Limit of Detection (LOD)	Medium used	Ref.
1.	$[Cd_3(CBCD)_2(DMA)_4(H_2O)_2]\cdot 10DMA$	4.47×10^4	145 ppb	DMA	*Dalton Trans*., **2019**, *48*, 2683–2691
2.	$\{Zn_4(TPOM)(1,4\text{-}NDC)_4\}_n$	2.74×10^4	0.28 ppm	water	*ACS Appl. Mater. Interfaces*, **2018**, *10*, 42406−42416
3.	$[Zn_2(L)_2(TPA)].\ 2H_2O$	2.36×10^4	0.39 ppm	Methanol	*New J. Chem*., **2019**, *43*, 2353−2361
4.	$[Ag(CIP^-)]$	5.2×10^4	105 ppb	DMF	*Dalton Trans.*, **2019**, *48*, 10892–10900
5.	$[Zn_3(DDB)(DPE)]\cdot H_2O$	3.3×10^4	166 ppb	water	*Dalton Trans*., **2019**, *48*, 16776–16785
	$[Mg_2(APDA)_2(H_2O)_3]\cdot 5DMA\cdot 5H_2O$	7.50×10^4	150 ppb	DMF	*Inorg. Chem*., **2018**, *57*, 13330−13340
6.	$[Zn_2(bpdc)_2(BPyTPE)]$	–	0.13 ppm	DCM	*Chem. Commun*., **2017**, *53*, 9975--9978
7(a)	**CSMCRI-8** for DCNA	$3.8 \times 10^4\ M^{-1}$	0.060 ppm/124 nM	DMF	**This work**
7(b)	**CSMCRI-8** for IPT	3.74×10^5	0.110 ppm/226 nM	DMF	**This Work**

References

1. Sheldrick, G., SAINT and XPREP, version 5.1. *J Siemens Industrial Automation Inc., Madison, WI* **1995**.
2. Sheldrick, G., SADABS, empirical absorption Correction Program. University of Göttingen: Göttingen, Germany1997.
3. Bruker, S., Bruker AXS Inc., Madison, Wisconsin, USA, Version 6.02 (includes XPREP and SADABS). **1999**.
4. Sheldrick, G., SHELXTL reference manual: Version 5.1. *J Bruker AXS, Madison, WI* **1997**.
5. Sheldrick, G., SHELXL-2014/7, University of Gottingen, Germany, 2014 Search PubMed;(b) L. Farrugia. *J. Appl. Crystallogr* **2012,** *45*, 849-854.
6. Spek, A., Single-Crystal Structure Validation with the Program Platon. *J. Appl. Crystallogr.* **2003,** *36*, 7-13.
7. Blatov, V.; Schevchenko, A., TOPOS, v4. 0; Samara State University, Samara, 2011.(b) Blatov, VA IuCr CompComm. Newsl2006.
8. Blatov, V. A.; Shevchenko, A. P.; Proserpio, D. M., Applied Topological Analysis of Crystal Structures with the Program Package ToposPro. *Cryst. Growth Des.* **2014,** *14*, 3576-3586.
9. Kühne, T. D.; Iannuzzi, M.; Ben, M. D.; Rybkin, V. V.; Seewald, P.; Stein, F.; Laino, T.; Khaliullin, R. Z.; Schütt, O.; Schiffmann, F.; Golze, D.; Wilhelm, J.; Chulkov, S.; Bani-Hashemian, M. H.; Weber, V.; Borštnik, U.; Taillefumier, M.; Jakobovits, A. S.; Lazzaro, A.; Pabst, H.; Müller, T.; Schade, R.; Guidon, M.; Andermatt, S.; Holmberg, N.; Schenter, G. K.; Hehn, A.; Bussy, A.;

Belleflamme, F.; Tabacchi, G.; Glöß, A.; Lass, M.; Bethune, I.; Mundy, C. J.; Plessl, C.; Watkins, M.; VandeVondele, J.; Krack, M.; Hutter, J., CP2K: An Electronic Structure and Molecular Dynamics Software Package - Quickstep: Efficient and Accurate Electronic Structure Calculations. **2020,** *152*, 194103–194150.
10. Perdew, J. P.; Burke, K.; Ernzerhof, M. Generalized GradientApproximation Made Simple. Phys. Rev. Lett. 1996, 77, 3865−3868.

11. VandeVondele, J.; Hutter, J., Gaussian basis sets for accurate calculations on molecular systems in gas and condensed phases. *J. Chem. Phys.* **2007,** *127*, 114105.
12. Goedecker, S.; Teter, M.; Hutter, J. Separable Dual-SpaceGaussian Pseudopotentials. Phys. Rev. B 1996, 54, 1703−1710.

13. Grimme, S.; Antony, J.; Ehrlich, S.; Krieg, H., A consistent and accurate ab initio parametrization of density functional dispersion correction (DFT-D) for the 94 elements H-Pu. *J. Chem. Phys.* **2010,** *132*, 154104.
14. Campañá, C.; Mussard, B.; Woo, T. K., Electrostatic Potential Derived Atomic Charges for Periodic Systems Using a Modified Error Functional. *J. Chem. Theory Comput.* **2009,** *5*, 2866-2878.
15. Krykunov, M.; Demone, C.; Lo, J. W. H.; Woo, T. K. A. New Split Charge Equilibration Model and REPEAT Electrostatic Potential Fitted Charges for Periodic Frameworks with a Net Charge. J. Chem. Theory Comput. 2017, 13, 2858−2869.

16. Rappe, A. K.; Casewit, C. J.; Colwell, K. S.; Goddard, W. A.; Skiff, W. M., UFF, a full periodic table force field for molecular mechanics and molecular dynamics simulations. *J. Am. Chem. Soc.* **1992,** *114*, 10024-10035.
17. Mayo, S. L.; Olafson, B. D.; Goddard, W. A., DREIDING: a generic force field for molecular simulations. *J. Phys. Chem.* **1990,** *94*, 8897-8909.
18. Harris, J. G.; Yung, K. H., Carbon Dioxide's Liquid-Vapor Coexistence Curve And Critical Properties as Predicted by a Simple Molecular Model. *J. Phys. Chem.* **1995,** *99*, 12021-12024.
19. Dubbeldam, D.; Calero, S.; Ellis, D. E.; Snurr, R. Q., RASPA: molecular simulation software for adsorption and diffusion in flexible nanoporous materials. *Mol. Simulat.* **2016,** *42*, 81-101.
20. Peng, D.-Y.; Robinson, D. B., A New Two-Constant Equation of State. *Ind. Eng. Chem. Fundamen.* **1976,** *15*, 59-64.
21. Vlugt, T. J. H.; García-Pérez, E.; Dubbeldam, D.; Ban, S.; Calero, S., Computing the Heat of Adsorption using Molecular Simulations: The Effect of Strong Coulombic Interactions. *J. Chem. Theory Comput.* **2008,** *4*, 1107-1118.
22. Donnay, J. D. H.; Harker, D., A new law of crystal morphology extending the Law of Bravais. *Am. Mineral.* **1937,** *22*, 446-467.
23. Friedel, G. J. B. d. M., Etudes sur la loi de Bravais. *Bull. Soc. Franc. Mineral* **1907,** *30*, 326-455.